A subpopulation of spinocerebellar tract neurons regulates the stability of bipedal stepping

Baruch Haimson[1], Yoav Hadas[1], Artur Kania[2], Monica Daley[3], Yuval Cinnamon[4], Aharon Lev-Tov[1,*] and Avihu Klar[1,*]

1 - Department of Medical Neurobiology, IMRIC, Hebrew University-Hadassah Medical School, Jerusalem, 91120, Israel
2 - Institut de recherches cliniques de Montréal (IRCM), Montréal, QC, H2W 1R7, Canada
3 - Ecology and Evolutionary Biology, University of California, Irvine, CA, USA
4 - Institute of Animal Science Poultry and Aquaculture Sci. Dept. Agricultural Research Organization, The Volcani Center, Israel

* - Corresponding authors

Avihu Klar

Department of medical Neurobiology

Hadassah Medical School

The Hebrew University, Jerusalem

91120

Israel

avihu.klar@mail.huji.ac.il

Aharon Lev-Tov

Department of medical Neurobiology

Hadassah Medical School

The Hebrew University, Jerusalem

91120

Israel

aharonl@ekmd.huji.ac.il

Summary

Peripheral and intraspinal feedback is delivered to the cerebellum through the spinocerebellar tracts in order to shape and update the output of spinal networks that execute motor behavior. However, genetic inaccessibility of the tract neurons prevented further elucidation of the ascending circuits. We report that genetically targeted lumbar dI2 interneurons, form a part of the avian ventral spinocerebellar tract. Lumbar dI2s receive synaptic input from afferents and pre-motoneurons. They innervate contralateral dI2s and pre-motoneurons at lumbar cord and their ascending axons give off collaterals to innervate contralateral brachial dI2s and premotoneurons, enroute to the cerebellum. Collectively these findings suggest that dI2s deliver peripheral and intraspinal feedback to the cerebellum, that they also function as interneurons in local lumbar circuits and involved in lumbo-brachial coupling. Targeted silencing of dI2s leads to destabilized stepping in P8 hatchlings, suggesting that the activated dI2s may contribute to stabilization of the bipedal gait.

Keywords: spinal cord, spinocerebellar tract, neuronal circuits, locomotion

Introduction

Coordinated, patterned movements generated by spinal rhythmogenic networks (central pattern generators) are initiated and modulated by descending supra-spinal pathways. Continuous proprioceptive-afferent information from muscles, tendons, and joints, enters the spinal cord through dorsal roots, integrated by different types of spinal neurons and delivered to spinal and supra-spinal targets [1]. The cerebellum is involved in the maintenance of the stability of the body and in the coordination, precision, and timing of movements. Anatomical and electrophysiological studies of cats and rodents revealed two major pathways ascending from tract neurons in the lumbar spinal cord to the cerebellum, the dorsal and the ventral spinocerebellar tract (DSCT and VSCT). DSCT tract neurons are considered to relay mainly proprioceptive information, while VSCT tract neurons are thought to relay internal spinal network-information to the cerebellum in addition to proprioceptive data [2-5].

Feline VSCT cells have been reported to be excitatory neurons, distributed at the L3-L6 segments. Their axons cross the ventral midline at the lumbar level and cross back at the cerebellum. VSCT neurons receive synaptic input from afferents, from inhibitory and excitatory premotoneurons, and descending rubrospinal, vestibulospinal, reticulospinal and medial longitudinal fasciculus fibers [2,6]. VSCT neurons also send collaterals to the contralateral lamina VII at the segmental level. VSCTs comprise a heterogeneous population of interneurons that vary in their soma location, extent of synaptic inputs from sensory afferents and supra-spinal descending neurons. They also vary in their projection pattern and peduncular entry to the cerebellum [2,4,7-11]. Similar features of VSCT neurons were also found in the chick lumbar spinal cord [12-16]. The genetic inaccessibility of DSCT and VSCT neurons hinders better understanding of their spinal and supra-spinal projections, their

connectome, their physiological properties, and their actual contribution to the regulatory functions of the cerebellum.

In order to define potential VSCT neurons within the progenitor population of spinal interneurons, we set the following criteria: 1) Soma location in accordance with pre-cerebellar neurons at the lumbar level, which were previously revealed by retrograde labeling experiments of the chick cerebellar lobes [12-14], 2) Commissural neurons, 3) excitatory neurons, and 4) non-premotoneurons [17-19]. Based on these criteria dI1c and dI2 neurons are likely candidates (Fig. S1B). This is further supported by Sakai et al., who demonstrated that in the E12 chick, dI1 and dI2 axons project to the hindbrain and toward the cerebellum [15]. dI2 neurons outnumber dI1c neurons, and are likely to be a major sub-population of VSCT neurons.

We have previously developed a circuit-deciphering toolbox that enables neuronal-specific targeting and tracing of neuronal circuits in the chick embryo [20]. The implementation of these tools revealed that dI2 neurons at the lumbar cord possess many features of VSCT neurons. We have applied new tools for manipulating neuronal activity in the chick spinal cord and for monitoring locomotion of genetically manipulated chick hatchlings, including genetic targeting of neuronal activity modifiers and stabilization of transgene expression at post-hatching stages. Utilizing these tools, we studied the circuitry dI2 neurons and their possible role in refinement of stepping of post-hatching chick. We found that lumbar dI2 neurons receive synaptic inputs from inhibitory and excitatory premotoneurons and relay output to the cerebellar granular layer and the medial cerebellar nucleus. The involvement of dI2 neurons in modulation of chick locomotion was studied by inhibiting their neuronal activity by targeted expression of the tetanus toxin gene and examining the overground stepping of the hatched chicks. Kinematic analysis of stepping of P8 hatchlings showed

unstable stepping in genetically manipulated hatchlings, hence demonstrating that dI2s play a role in shaping the avian bipedal gait.

Results

dI2 are commissural neurons that project to the cerebellum.

The dI2 neurons are the 2nd dorsal population of spinal interneurons. Neither the progenitors nor the post mitotic dI2 can be defined by expression of dI2-specific transcription factors (TFs). Rather, a combination of TFs (expressed also in other interneurons) defines their identity [19,21,22]. dI2 neurons, axons, and terminals were labeled using intersection between Ngn1 and the Foxd3 enhancers (Fig. S1A) [20,23]. At E5, the post mitotic dI2 neurons migrate ventrally from the dorso-lateral to the mid-lateral spinal cord (Fig. 1A). At E6, dI2 neurons assume a mid-lateral position along the dorso-ventral axis (Fig. 1B). Subsequently, dI2 neurons migrate medially, and at E17, they occupy lamina VII (Fig. 1C). At all rostro-caudal levels and embryonic stages, dI2 axons cross the floor plate (Fig. 1A-D). Post-crossing dI2 axons extend rostrally for a few segments at the ventral funiculus (VF) and subsequently turn into the lateral funiculus (LF) [23] (Fig. 1C). The VF to LF rerouting is apparent at the rostral thoracic levels (Fig. 1D). Collaterals originating from the crossed VF and LF tracts invade the contralateral spinal cord (Fig. 1C, D).

A recent study suggested that dI2 neurons at early stages of development in mice (e9.5-e13.5) can be divided into several sub classes based on their genetic signature, and degree of maturation [24]. To assess the diversity of dI2 neurons in the chick, the expression of dI2 TFs was analyzed at E5 before and during ventral migration, E6 and E14, dI2::GFP cells. The pre-migratory post mitotic dI2::GFP are a homogenous population defined by Foxd3$^+$/Lhx1$^+$/Pou4f1$^+$/Pax2$^-$ (Fig. 1E, S2A,B). The dI2 neurons that undergo ventral migration at E5, as well as at E6 and E14, express variable combinations of Lhx1, Pou4f1 and FoxP1/2/4 (Fig. 1E, S2C,D). At E14, about 50% of dI2::GFP did not express any of the tested TFs (Fig. 1E), suggesting that the early expression of TFs is required for cell fate acquisition, axon

guidance, and target recognition, while their expression is redundant during circuitry formation, as shown for other spinal INs [25]. Interestingly, about 12% of ventrally migrating dI2 neurons (from E5 to E14) express Pax2 (Fig. 1E, S2D). Pax2 is associated with inhibitory phenotype [26], suggesting that a subpopulation of dI2 are inhibitory neurons. The distribution of excitatory and inhibitory dI2 neurons is also apparent at E17. *In situ* hybridization on cross sections of E17 dI2::GFP-labeled lumbar spinal cord, the vGlut2 probe revealed that 88% were vGlut2$^+$, while the Gad1 probe measured 25% Gad1$^+$ dI2 neurons (Fig. S3A-D). A similar percentage of Gad2 and Slc6a5 dI2-expressing cells were found also in mouse [24].

At E13-17 in the caudal lumbar level and in the level of the sciatic plexus, most dI2 neurons reside at the medial aspect of lamina VII. About 91% of dI2 neurons are small-diameter neurons that reside at the lateral dorsal aspect of lamina VII, and 9% are large-diameter neurons. At the lumbar sciatic plexus level, large-diameter dI2 neurons mostly reside at the ventral aspect of lamina VII and at the level of the crural plexus in the dorsal aspect of lamina VII (Fig. 1F,G; Fig. S3E). A similar distribution of dI2 neurons is apparent also at the thoracic and brachial levels (Fig. S3E-F). Importantly, large-diameter dI2 neurons are only apparent at the lumbar level (Fig. 1F, S3E-F). The division of large- and small-diameter lumbar dI2 neurons was not reflected in the expression of the tested TF.

To study the supra-spinal targets of dI2 neurons, axonal and synaptic reporters were expressed in lumbar dI2 neurons (Fig. 2A). At E17, the stage in which the internal granule layer is formed in the chick cerebellum, the axons and synapses of dI2 neurons were studied in cross sections. dI2 axons cross the spinal cord at the floor plate at the segmental level, ascend to the cerebellum, enter through the superior cerebellar peduncle, and cross back to the other side of the cerebellum ipsilaterally to the targeted dI2s (Fig. 2B). Synaptic boutons are noticeable in the granule layer at the ipsilateral and contralateral sides of the anterior

cerebellar lobules (Fig. 2C). Synapses were also present in the central cerebellar nuclei (Fig. S4A).

The difference in the soma size between the dorsally and ventrally located dI2 neurons prompted us to test which dI2 neurons project to the cerebellum. The dI2 and pre-cerebellar neurons were co-labeled by genetic targeting of dI2 at early stages of embryogenesis (E3), coupled with intra-cerebellar injection of cholera toxin subunit B (CTB) or replication-defective HSV-LacZ at E15 (Fig. 2A). Only large-diameter neurons were co-labeled, most of them in the ventral aspect of lamina VII (Fig. 2D,E,H; S4B,C). Interestingly, many of CTB^+ or $LacZ^+$ neurons were contacted by dI2 axons (Fig. 2F,G,I; S4D,E), suggesting that small-diameter dI2 neurons innervate pre-cerebellar neurons.

dI2 neurons receive synaptic input from pre-motoneurons and sensory neurons

To assess the synaptic input to dI2 neurons we investigated their synaptic connectivity with dorsal root ganglion (DRG) neurons, pre-motoneurons, and reticulospinal tract neurons. Two genetically defined pre-motoneurons were examined: V1 – inhibitory pre-motoneurons population [25,27] and dI1i excitatory INs. A density plot of dI1 synapses shows dI1i terminals within the motoneurons zone (lamina IX) and at lamina VII (Fig. 3C). Co-labeling of motoneurons and dI1 synapses revealed synaptic contacts of dI1i on motoneurons (Fig. S5A-B). This was further supported by co-labeling dI1 with pre-MNs via hindlimb injection of pseudorabies virus (PRV) (Fig. S5C-D).

To identify dI2 presynaptic neurons we applied two criteria: co-distribution of axonal terminals from the presumed presynaptic neurons and the soma of dI2, and detection of synaptic boutons on the somatodendritic membrane of dI2 neurons. The dI2, DRG, V1, and dI1 neurons were labeled using specific enhancers (Fig. S1). General pre-motor INs were

labeled by injection of PRV-cherry virus into the ipsilateral hindlimb musculature [20] (Fig. 3B). A density profile of the axons of DRG neurons (Fig. 3A, S6A-D) and PRV-labeled pre-MNs (Fig. 3B), and a density profile of synaptic boutons from dI1i (Fig. 3C, S6E), V1 (Fig. 3D), and reticulospinal tract neurons ($5HT^+$ synapses) (Fig. 3E, S6F) were aligned to the density scheme of the somata of dI2 neurons. The overlap between the axonal terminals of DRG neurons, PRV-labeled pre-motoneurons, dI1i and V1 boutons, and the somata of dI2 neurons is evident (Fig. 3A-F, Fig. S6G). To further substantiate these synaptic connections, we performed double labeling of DRG, PRV-labeled pre-motoneurons, V1, and dI1i, together with dI2 neurons. Contact between DRG axons and dI2 neurons was mainly apparent in the dorsal dI2 neurons, while the ventral dI2 neurons received little to no input from DRG neurons (Fig. 3A, S6A,B). Synaptic connections, evaluated by boutons on dI2 dendrites and somata, are apparent from the pre-motor neurons V1 and dI1i (Fig. 3C,D). Serotonergic synapses were found to be concentrated on motoneurons and did not overlap with dI2 neurons (Fig. 3E, S6F). Double-labeling of 5HT and dI2 neurons did not reveal any synaptic input.

The analysis of the synaptic inputs supports the concept that dI2 neurons constitute part of the VSCT, and that they receive input from inhibitory and excitatory pre-motoneurons and project to the cerebellum. The cellular distribution of the axons of large-diameter dI2 neurons in the ventral (Fig. 1G, S3E) and dorsal (S3E) spinal cord suggests that they constitute the Ib and VII-VSCT, described in cats [4]. The lack of synaptic serotonergic input may be related to the difference in species, or in the VSCT subfamily, or to non-dI2 VSCT neurons residing adjacent to motoneurons.

dI2 neurons innervate contralateral lumbar and brachial pre-MNs and dI2 neurons

Axon collaterals of dI2 invade the spinal cord gray matter along the entire length of the spinal cord, as revealed by whole mount staining of spinal cords electroporated with alkaline phosphatase reporter (dI2::AP) (Fig. 4A) and membrane-tethered EGFP (Fig. 4B). The region innervated by dI2 collaterals (arrow at Fig. 4B) overlap with that of the pre-MNs, V0 and V1 [17,28], as well as with that of the contralateral dI2 neurons (Fig. 1, Fig. 4B). To assess the potential spinal targets of dI2 neurons, the density of dI2 synapses was aligned to dI2 (Fig. 4C), the ipsilateral pre-MNs (Fig. 4D), and contralateral pre-MNs (Fig. 4E). The alignment revealed a significant overlap of dI2 synapses and ipsi/contralateral pre-MNs with dI2 neurons (Fig. 4G,H). Co-labeling of synaptic dI2 coupled with labeling of the above neuronal population showed dI2 synaptic boutons on pre-MNs and dI2 neurons at the lumbar level (Fig. 4C-H, S7A-C).

The pattern of dI2 collaterals along the entire rostrocaudal axis (Fig. 4A) suggests that dI2 neurons innervate contralateral pre-MNs and dI2 neurons at multiple levels. To test this, labeling of lumbar dI2 neurons was coupled with labeling of brachial pre-MNs and dI2 soma labeling via wing musculature injection of PRV or electroporation of reporter in brachial dI2 neurons, respectively (Fig. 4F, S7D). dI2-synapses and the putative targets overlapped, and synaptic boutons originated from lumbar level dI2 neurons are apparent on dI2 neurons, and on the contra- and ipsilateral pre-MNs of the wings (Fig. 4F, S7D-F).

The circuit mapping experiments showed that lumbar dI2 neurons innervate the cerebellum, lumbar and brachial pre-MN, and contralateral dI2 (Fig. 6D). Hence, dI2 neurons may relay peripheral and intraspinal information to the cerebellum and to the contralateral lumbar and brachial motor control centers.

Targeted silencing of dI2 neurons impairs stability of bipedal stepping

To study the physiological role of dI2 neurons, we silenced their activity using bilateral targeting of the tetanus toxin (*TeTX)* gene, to lumbar dI2s. EGFP was co-targeted in a 2/1 TeTX/EGFP ratio. EGFP expression in dI2 neurons and none-electroporated chicks was used as a control. In order to maximize the number of targeted dI2 neurons, we combined genetic targeting with the *Foxd3* enhancer and spatial placement of the electrodes at the dorsal spinal cord (Fig. S1A). Embryos were electroporated at Hamburger-Hamilton (HH) stage 18 and incubated in a rotating incubator. Upon hatching, chicks were imprinted on the trainer and trained for targeted over ground locomotion.

At P8, the weight of the chicks was measured and the feet grip power evaluated (see below). Gait parameters of two controls and 5 *TeTX* treated chicks were measured while chicks were walking toward their imprinting trainer along a horizontal track (6-20 walking sessions, 5-8 strides each, per chick). Following the experiments, chicks were scarified and their spinal cords were removed and processed for immune-detection of the efficacy of the electrophoresis (Supplementary table S1).

The weight of all chicks was comparable within the range of 140.6±10.6 gr (Supp. Table S1). As a functional measure of foot grip, we tested the ability of the chicks to maintain balance on a tilted meshed surface. *TeTX*-manipulated chicks and control chicks, maintained balance on the titled surface up to 63–70^0, with no apparent statistically significant differences (Supplementary Table S1, Supplementary statistics).

Analysis of over ground locomotion of the control and *TeTX* treated chicks revealed substantial differences. *TeTX* chicks exhibited whole-body collapses during stepping (Fig.

5B,C, Fig. 6A), wide-base stepping (table 2), decreased swing velocity (table 1) and variable limb movements (Fig.5 D,E, Fig. 6B,C, tables 3,4, Supplementary statistics).

Whole-body collapses: A collapse was scored as a decline of the knee height below 85% of the average knee height at the stance phase of the step (arrow in Fig. 5C). Collapses were usually followed by over-extensions (arrow head in Fig. 5C). We measured the number of collapses in 50–190 steps. In control chicks, collapses occurred in 0–2.12% of the steps. In one of the *TeTX* manipulated chicks (*TeTX1*) we observed collapses in 4.4% of the steps and in the other four *TeTX*-manipulated chicks, collapses were scored in 18–29% of the steps, significantly different from the controls (Fig. 6A, Supplementary statistics). The collapses and over-extensions were also manifested in the profiles of the knee height trajectory during the swing phase (Fig. 5D).

Wide base stepping: Wide-base stance is typical to unbalanced ataxic gait. The stride width was measured between the two feet during the double stance phase of stepping. The mean stride in *TeTX*-manipulated chicks 1,2,4, and 5 was significantly wider than the control chicks, while the width in *TeXT3* was similar to the controls (Table 2,-Supplementary statistics).

Decreased swing velocity: The speed of locomotion, calculated as the swing velocity, varied between different sessions in each chick and between chicks. However, the swing velocity in control1 was significantly higher, than the other chicks (table 1, Supplementary statistics). An 180^0 out-of-phase striding pattern was found during stepping in all the manipulated and the control chicks (Fig. S8A, table 1, Supplementary statistics).

Variable limb movements: In stable gait, limb trajectories are consistent from stride to stride. For point by point comparisons of the trajectories in knee height and angles of the TMP joint during the swing phase of stepping in control and TeTx manipulated chicks, the

swing phase was normalized using 126 consecutive epochs, and the data were displayed as a function of the percentage of swing (0-100%). Plots of the knee height and TMP angle trajectories during the normalized swing in all the analyzed steps of each chick are shown superimposed in Fig. 5D and Fig. 5E, respectively. These data demonstrate that the range of changes in *TeTX*-manipulated chicks was higher comparing to control chicks.

Further analyses (Fig. 6B) revealed that the mean range of the knee height in each of the *TeTx* manipulated chicks was significantly higher than that of each of the control chicks (Fig. 6B; One-way ANOVA followed by Dunnett's multiple comparison, Supplementary statistics). Similar comparison of the range of angular excursions of the TMP joint during the normalized swing are shown as a box whisker plot and as circular display of the mean vectors of the control and TeTx manipulated chicks in Fig. 6C left and right, respectively. The mean range of angles of the TMP joint of controls were significantly smaller comparing to each of the *TeTX* manipulated chicks (Watson and Williams F test, followed by pairwise comparisons). (Fig. 6C, Supplementary statistics).

Since the increased range of changes could be due to the effects of the substantial increase in body collapses during stepping (Fig. 6A, see also Fig. 5), we excluded steps featuring whole body collapses and reanalyzed the data. The data summarized in table 3, shows that the significant difference between controls and the *TeXT*-treated chicks in the range of the knee height and the TMP angle excursions was maintained. Thus, the increase in irregularity in the *TeXT*-treated chicks is not only due to the body collapses of the *TeXT*-treated chicks.

In coordinated gait, the elevation and lowering of the foot during the swing phase can be demonstrated by the correlations between the height of the foot and the angles of the leg joints. A decrease in the correlations, leading to perturbed gait, can stem from the

following events: collapses - an increased flexion of the ankle and TMP joints without elevation of the foot; an over-extension of the legs - an enlargement of joints extension without elevation of the foot; widening of the step or an elevation of the foot by a lateral shift of the leg with a reduced contribution of the joints. We analyzed the correlations between the height of the TMP joint (as a proxy of the height of the foot), and the angles of the ankle and TMP joints during the descending phase of the swing. In the control chicks, the angle of the TMP joint was positively correlated with the height of the TMP joint (angular to linear correlation). While the angle of the ankle joint was negatively correlated with the angle and height of the TMP joint (angular to angular correlation) (Table 4, Fig S8B, Supplementary statistics). A substantial decrease in the correlations between the TMP height and TMP angle, as well as between TMP height and the ankle angle, were evident in the *TeTX*-treated chicks, while the correlation between the TMP and the ankle angles was not affected (Table 4, Fig S8B, Supplementary statistics). The reduction in correlations between foot elevation and joints flexion and extension is an additional manifestation of unstable gait in *TeTX*-treated chicks, displayed by collapses, over-extensions, and step-widening.

Discussion

The VSCT in mammals is thought to provide peripheral and intrinsic spinal information to the cerebellum in order to shape and update the output of spinal networks that execute motor behavior. The main findings in our study are that dI2 neurons in the chick lumbar spinal cord form a part of the avian VSCT, and that targeted silencing of dI2 neurons leads to impaired stepping in P8 hatchlings. We described the spatial distribution of sub-populations of dI2 neurons, deciphered their connectomes, mapped the trajectory of their projection to the cerebellum, and suggested possible mechanisms for the perturbed gait resulted from their genetic silencing, as discussed below.

We have shown that dI2 neurons in the chick spinal cord, are excitatory commissural neurons that innervate granule neurons in the ipsilateral cerebellum after double crossing the midline. We demonstrated that lumbar dI2s receive sensory innervation, pre-motor inhibitory and excitatory innervation, and innervation from contralateral lumbar dI2s (Fig. 6D). Thus, lumbar dI2 neurons can provide the cerebellum proprioceptive information, copies of motor commands delivered from pre-motoneurons, and integrated information from contralateral dI2 neurons.

Using the intersection between genetic drivers and spatially restricted delivery of reporters to defined lumbar and brachial neurons, we have identified several targets of dI2 lumbar neurons. Ipsilateral lumbar dI2 neurons innervate contralateral lumbar dI2 neurons as well as commissural and non-commissural lumbar pre-motoneurons. This connectivity may affect the bilateral spinal output circuitry at the lumbar cord (e.g. [2,6]) Moreover, the ascending axons of lumbar dI2s, give off grey matter collaterals innervating contralateral dI2s and commissural and non-commissural pre-motoneurons throughout the brachial spinal cord (Fig. 6D). Therefore, lumbar dI2 neurons may also contribute to the inter-

enlargements coupling described between the limb and wing moving segments of the spinal cord (e.g. [29,30] for forelimb to hindlimb coupling connectivity in mice}.

The unclear genetic origin of physiologically equivalent lumbar VSCT neurons, prevented better understanding of their role in hindlimb locomotion. Our wiring and neuronal-silencing studies implicated dI2 as a significant contributor to the regularity and stability of locomotion in P8 hatchlings. The kinematic analysis of TeTX treated hatchlings, revealed imbalanced locomotion with occasional collapses, increased stride variability, wide base stepping, and loss of correlations between joints heights and angles during stepping.

The mechanisms accounting for the impaired stepping following dI2 silencing are still unknown. One of the suggested mechanisms is that silencing the dI2s perturbs the delivery of peripheral and intrinsic feedback to the cerebellum, leading to unreliable updating of the motor output produced by the locomotor networks, thereby impairing the bipedal stepping.

Another possible mechanism is based on the similarity of the gait instabilities of TeTX treated hatchlings to ataxic motor disorders. Mammalian VSCT neurons receive descending input from reticulospinal, rubrospinal and vestibulospinal pathways [2,6]. Neurons from the lateral vestibular nucleus, have been reported to innervate extensor motoneurons at the lumbar level, as well as interneurons residing at the medial lamina VII [31], exactly at the location where dI2 neurons were found to reside in our study. Thus, the vestibulospinal tract may convey input directly to the ipsilateral motoneurons, and indirectly to contralateral motoneurons through dI2 neurons that innervate contralateral pre-motoneurons. This way silencing of dI2 neurons is expected to interfere with the descending regulation of the stability of the bipedal gait.

In summary, our mapping studies of dI2 neurons and their connectomes followed by characterization of the effects of their silencing on bipedal stepping, offer new insights on

the function of VSCT neurons in vertebrates. We suggest that lumbar VSCT neurons are not merely used to relay sensory and intrinsic spinal networks information to the cerebellum, but also act as active mediators of motor functions at the lumbar segments and at the wing controlling brachial segments of the spinal cord. Moreover, our studies suggest a gait stabilizing role to vestibulospinal connectivity onto lumbar dI2 neurons. Further circuit deciphering studies of the constituents of sub-populations of dI2s, their targets, and their descending inputs are required to extend our understanding of the function of VSCT neurons in motor control of movements.

Acknowledgements: The authors thank Haya Falk for PRV purification; Alona Katzir, Cole Bendor, Mevaseret Avital, Sapir Shevah, Eitan Yisraeli, Ruth Segal, Fedaa Bazan and Eden Kimchi for technical assistance. This work was supported by grants to AK from the Israel Science Foundation (grant No. 1400/16), The US-Israel Binational Science Foundation (grant No. 2017/172) and the Avraham and Ida Baruch endowment fund.

Author contributions:

B.H., A.Klar and ALT designed research; B.H., and Y.H. preformed research; B.H., and M.D. generated the kinematic analysis tools; Y.C. assisted in the post hatching analysis; A. Kania provided reagents and comments on the research; B.H., A.Klar and ALT analyzed the data; B.H., A.Klar and ALT wrote the paper.

Competing Interests:

The authors declare no competing interests.

Material & correspondence:

Avihu Klar

Department of medical Neurobiology
Hadassah Medical School
The Hebrew University, Jerusalem
91120
Israel
avihu.klar@mail.huji.ac.il

Figure legends

Figure 1: Characterization and classification of dI2 neurons during embryonic development. dI2 interneurons were labeled by genetic intersection between Foxd3 and Ngn1 enhancers [23] (Supp Fig. S1).

A–D. dI2 axonal projection during development. At E5 (A) post mitotic dI2 neurons assume a dorsolateral position and start to migrate ventrally. At E6 (B) dI2 neurons occupy the mid-lateral domain. At E15-17 dI2 neurons are located at the medial lamina VII at the lumbar level (LS3) (C) and the thoracic level (T1) (D). dI2 axons cross the floor plate (yellow arrowheads), turn longitudinally at the ventral funiculus (white arrowheads) and eventually elongate at the lateral funiculus (white arrows).

E. A graph indicating the fraction of dI2 neurons expressing TFs during development. **F.** Cross section of an E17 embryo at the lumbar spinal cord (crural plexus level, LS2). Small-diameter dI2 neurons residing in lamina VII (F') and ventromedial large-diameter dI2 neurons in lamina VIII (F"). **G.** Density plots of dI2 somata in the sciatic plexus level (*N*=374 cells), $dI2_{large}$ (magenta) and $dI2_{small}$ (yellow) INs in the (*N*=33 and *N*=344 cells, respectively).

See Figure S2 and S3.

Figure 2: dI2 neurons project to the cerebellum.

A. Experimental setup for labeling of cerebellar projecting dI2 neurons. dI2 neurons were genetically targeted at HH18, and pre-cerebellar neurons were labeled using intra-cerebellar injection of CTB or replication defective HSV-LacZ at E15. **B.** A cross section of E17 brainstem and cerebellum. The dashed polygon in B' is magnified in B. dI2 axons reach the cerebellum, enter into it via the superior cerebellar peduncle and cross the cerebellum midline. Calbindin (Purkinje neurons, magenta), synaptotagmin (yellow). **C.** A cross section of E17 cerebellar

cortex. Lumbar dI2 synapses (cyan) in the granular layer of the anterior cerebellar cortex. Calbindin (Purkinje neurons, magenta), synaptotagmin (yellow). **D.** A cross section of an E15 embryo at the lumbar spinal cord level (sciatic plexus level). Pre-cerebellar neurons were infected and labeled by HSV-LacZ (magenta), and dI2 neurons express GFP (cyan). A large-diameter dI2 neuron is co-expressing LacZ and GFP (magnifications of the two channels in the insets). **E.** Density plots of dI2 and pre-cerebellar neurons (density values 10-90%) in the sciatic plexus segments (*N*=374 and *N*=289 cells, respectively). **F.** CTB labeled pre-cerebellar neuron (magenta) is contacted by dI2 axonal terminals (cyan). **G.** Density plots of dI2 synapses and pre-cerebellar neuron somata (density values 10-90%) in the sciatic plexus segments (*N*=4735 synapses and *N*=289 cells, respectively). **H,I.** Quantification of the overlap in area and volume of the two densities plots.

See Figure S4.

Figure 3: Synaptic inputs to dI2 neurons.

Schematic representations of the experimental design for labeling dI2::GFP or dI2::cherry INs (cyan) and potential sources of synaptic inputs (yellow or magenta), supplemented by cell soma density of dI2 INs and the synaptic densities are illustrated in A, B, C, D, E. The density values presented are 10-80%, 20-80%, 25-80%, 30-50% and 20-80%, respectively.

Examples of dI2 neurons contacted by axons or synaptic boutons are shown in A', B', C', and D'; and their 3D reconstruction in A'', B'', C'', and D''. Genetic labeling was attained using specific enhancers (Fig. S1) electroporated at HH18.

A. DRG neurons form contacts on dI2 neurons. Inset in A: cross section of and E17 embryo at the crural plexus level of the lumbar cord. A dorsally located dI2 neuron contacted by numerous sensory afferents, magnified in A' and 3D-reconstructed in A''. (*N*=18 sections)

B. Premotoneurons form contacts on dI2 neurons. dI2 neurons were labeled at HH18. At E13, PRV virus was injected to the leg musculature, and the embryo was incubated until premotoneurons infection (39 hours) (*N*=34 sections).

C. dI1 neurons form synapses on dI2 neurons. (*N*=8568 synapses).

D. V1 neurons form synapses on dI2 neurons. (*N*=1923 synapses).

E. dI2 neurons do not have 5HT synaptic terminals (*N*=1718 synapses). E17 cross sections of dI2::GFP labeled embryos were stained for 5HT.

F. Quantification of the overlap area of the different input sources and dI2 neuron densities plots.

See Figure S5, S6.

Figure 4: Spinal synaptic targets of dI2 neurons.

A. A whole mount staining of spinal cord (thoracic segments) expressing alkaline phosphatase (AP) in dI2 neurons. The lumbar dI2 neurons (not included in the image) were labeled with AP. dI2 axonal collaterals project and into the spinal cord (arrows).

B. Cross section of an E17 embryo at the crural plexus level of the lumbar cord. The axonal collaterals (white arrow) penetrating the gray matter of the contralateral side are evident. Schematic representations of the experimental design for labeling synapses (dI2::SV2-GFP, yellow) and potential targets (magenta) supplemented by cell soma density and dI2's synaptic densities are illustrated in C, D, E, and F. Examples of target neurons contacting synaptic boutons of dI2 neurons are shown in C', D', E', and F'; and their 3D reconstruction in C'', D'', E'', and F''. Genetic labeling was attained using dI2 enhancers (Fig. S1) electroporated at HH18. Pre-MNs were labeled by injection of PRV-cherry into the hindlimbs

(D, E) or the forelimb (F) musculature, at E13. The embryos were incubated until pre-MNs infection (39 hours).

C. dI2 neurons innervate the contralateral dI2 neurons (*N*=4735 synapses and *N*=374 cells, respectively).

D. dI2 neurons innervate ipsilateral projecting premotoneurons at the sciatic plexus level (*N*=4735 synapses and *N*=936 cells, respectively).

E. dI2 neurons innervate contralateral projecting premotoneurons at the sciatic plexus level (*N*=4735 synapses and *N*=47 cells, respectively).

F. dI2 neurons innervate brachial ipsilateral projecting premotoneurons (*N*=2215 synapses and *N*=286 cells, respectively).

G. Quantification of the overlap area of different synaptic targets and dI2 synapse density plots, as the percentage of overlap between dI2 synapses and the target.

H. Quantification of the overlap in volume of the different synaptic targets and dI2 synapse density plots, as the percentage of overlap between the synaptic target and dI2 synapses. See Figure S7.

Figure 5: Kinematic analysis of locomotion in post-hatching chicks following neuronal silencing of dI2.

A. Schematic illustration of chick hindlimb joints (bold) and bones (regular). The knee joint connects between the femur and the tibiotarsus, the ankle connects the tibiotarsus and the tarsometatarsus which connects to the phalanges by the tarsometatarso-phalangeal joint (TMP). During the swing phase of birds, the ankle flexion leads to elevate the foot, while the knee is relatively stable.

B,C. Stick diagrams of stepping in a control chicken d2::GFP (B) and in a d2::TeTX chicken (C). Arrows indicate falls and overshoots are denoted by arrowheads.

D. Overlays of knee height trajectories during the swing phase in all analyzed steps of each of the control and *TeTX* treated P8 hatchlings are shown superimposed with the respective 20%–80% color coded density plots as a function of the percentage of swing. (see Text and Materials and Methods). Arrows indicate falls and overshoots are indicated by arrowheads.

E. Overlay of angular trajectories of the TMP joint during the swing phase in all analyzed strides of each of the control and *TeTX* treated P8 hatchlings are shown superimposed with the respective 20%–80% color coded density plots as a function of the percentage of swing (see Text and Materials and Methods).

Figure 6. Increased variability in steps and decreased correlations between joints angle and height in *TeTX*-treated chicks.

A. The percentage of steps with body collapses in the controls and *TeTX* manipulated hatchlings.

B. Analysis of the mean range of knee height changes during the swing phase of control and TeTX treated chicks. All chicks were compared to control1, which is demarcated as a red circle. Circles for means that are significantly different either do not intersect, or intersect slightly, so that the outside angle of intersection is less than 90 degrees are shown in gray. If the circles intersect by an angle of more than 90 degrees, or if they are nested, the means are not significantly different and are shown in red. An alpha of 0.05 was used. For the knee height analyses, the number of steps was taken into account. (for further details see Text)

C. Analysis of the mean range of TMP angular excursions during the swing phase of control- and TeTX-treated chicks. (for further details see Text)

D. Schematic illustration showing the connectome of lumbar dI2 neurons. dI2s (magenta) receive synaptic input from sensory afferents (solid blue line indicates massive synaptic input and dashed blue line indicates sparse innervation), Inhibitory and excitatory premotoneurons (yellow), and from the contralateral lumbar dI2. dI2s innervate the contralateral lumbar and brachial premotoneurons (both commissural and ipsilateral projecting premotoneurons are innervated by dI2), the lumbar and brachial contralateral dI2, lumbar pre-cerebellar neurons (green) and the granule neurons in the cerebellum. See Figure S8.

Materials and Methods

Animals

Fertilized White Leghorn chicken eggs (Gil-Guy Farm, Israel) were incubated in standard conditions at 38 °C. All experiments involved with animals were conducted in accordance with the designated Experiments in Animals Ethic Committee policies and under its approval.

In-ovo electroporation

A DNA solution of 5 mg/mL was injected into the lumen of the neural tube at HH stage 17–18 (E2.75-E3). Electroporation was performed using 3 × 50 ms pulses at 25–30 V, applied across the embryo using a 0.5-mm tungsten wire and a BTX electroporator (ECM 830). Following electroporation, 150–300 µL of antibiotic solution, containing 100 unit/mL penicillin in Hank's Balanced Salt Solution (Biological Industry, Beit-Haemek) was added on top of the embryos. Embryos were incubated for 3–19 days prior to further treatment or analysis.

Immunohistochemistry and *In situ* hybridization

Embryos were fixed overnight at 4°C in 4% paraformaldehyde/0.1 M phosphate buffer, washed twice with phosphate buffered saline (PBS), incubated in 30% sucrose/PBS for 24 h, and embedded in OCT (Scigen, Grandad, USA). Cryostat sections (20 µm). Sections were collected on Superfrost Plus slides and kept at −20°C. For 100-µm sections, spinal cords were isolated from the fixed embryos and subsequently embedded in warm 5% agar (in PBS), and 100µm sections (E12–E17) were cut with a Vibratome. Sections were collected in wells (free-floating technique) and processed for immunolabeling.

The following primary antibodies were used—rabbit polyclonal GFP antibody 1:1000 (Molecular Probes, Eugene, Oregon, USA), mouse anti-GFP 1:100, Goat anti-GFP 1:300 (ABcam), rabbit anti-RFP 1:1000 (Acris), goat ChAT antibody 1:300 (Cemicon, Temecula, CA, USA), mouse anti-synaptotagmin antibody 1:100 (ASV30), mouse anti-Lhx1/5 1:100 (4F2), mouse anti-FoxP4 1:50 (hybridoma bank, University of Iowa, Iowa City, USA), mouse anti Brn3a 1:50 (Mercury), rabbit anti-Pax2 antibody 1:50 (ABcam), chicken anti-lacZ antibody 1:300 (ABcam), rabbit anti Clabindin 1:200 (Swant), rabbit VGUT2 antibody (Synaptic Systems, Göttingen, Germany), goat anti FoxP2 1:1000 (ABcam), goat anti FoxP1 1:100 (R&D Systems) and rabbit anti 5HT 1:100 (Immunostar). The following secondary antibodies were used: Alexa Fluor 488/647-AffiniPure Donkey Anti mouse, rabbit and goat (Jackson) and Rhodamin Red-X Donkey Anti mouse and rabbit (Jackson). Images were taken under a microscope (Eclipse Ni; Nikon) with a digital camera (Zyla sCMOS; Andor) or a confocal microscope (FV1000; Olympus).

In situ hybridization was performed as described (Avraham O et al., 2010). The following probes were employed: Foxd3, vGlut2 and GAD1 probes were amplified from a cDNA of E6 chick embryo using the following primers. Foxd3: forward-TCATCACCATGGCCATCCTG and Reverse -GCTGGGCTCGGATTTCACGAT. vGlut2: forward -GGAAGATGGGAAGCCCATGG and Reverse -GAAGTCGGCAATTTGTCCCC. GAD1: forward-TCTCACCTGGAGGAGCCATC and Reverse -CCTGAGGCTGATATCCAACC. T7 RNApol cis-binding sequence was added to the reverse primers.

AP staining

The treated embryos were fixed with 4% paraformaldehyde–PBS for 24 h at 4°C, and washed twice with PBS for 30 min at 4°C. The fixed embryos were incubated at 65°C in PBS

for 8 to 16 h to inactivate the endogenous AP activity. The treated embryos were washed with 100 mM Tris–Cl (pH 9.5) containing 100 mM NaCl and 50 mM MgCl2, and the residual Placental alkaline phosphatase activity was visualized by incubating the embryos with NBT/BCIP (Roche) in the same buffer at 4°C for 24 h. After extensively washing the embryos with PBS–5 mM EDTA, the spinal cord was imaged.

PRV infection

We used two isogenic recombinants of an attenuated PRV strain Bartha (PRV Bartha) that express enhanced GFP (PRV152) and monomeric red fluorescent protein (PRV614). The viruses were harvested from Vero cell cultures at titers 4 × 108, 7 × 108 and 1 × 109 plaque forming units (pfu/mL), respectively. Viral stocks were stored at −80°C. Injections of 3 µL of PRV152 or PRV614 were made into the thigh musculature of E13 or E14 chick embryos, using Hamilton syringe (Hamilton; Reno, NV, USA) equipped with a 33-gauge needle. The embryos were incubated for 36–40 h and sacrificed for analysis. For spinocerebellar projecting neurons labeling, we used a replication defective HSV (TK^-) that contains a lacZ reporter. The virus was injected *in ovo* into the cerebellum of E12-15 embryos, and the embryos were further incubated for 40–48. Alternatively, cholera toxin subunit B (CTB) conjugated to Alexa Fluor™ 647 (ThermoFisher) was used for the same purpose, and was injected to the cerebellum of E12–15 embryos together with the virus for visualization of both cerebellar projecting neurons and upstream neurons.

3D reconstruction and density plots analysis

The codes for both 3D reconstruction and the density plots analysis were written in Matlab. The density plots were generated based on cross section images transformed to a standard form. The background was subtracted, and the cells were filtered automatically based on

their soma area or using a manual approach. Subsequently, two-dimensional kernel density estimation was obtained using the MATLAB function "*kde2d*". Finally, unless indicated otherwise, a contour plot was drawn for density values between 20% and 80% of the estimated density range, in six contour lines.

Behavioral tests and analysis

The embryos were bilaterally electroporated, and were then let to develop and hatch in a properly humidified and heated incubator. Afterwards, within 32 hours post hatching, the hatchling chicks were imprinted on the trainer. The P8 chicks were filmed in slow motion (240 fps) freely walking (side and top views). The following parameters were scored: 1) weight, 2) foot grip power, 3) kinematics parameters during overground locomotion: a) swing velocity, b) swing and stance duration, c) phase of footfalls, d) height of knee and tarsometatarso-phalangeal (TMP) joints, e) angles of the TMP and ankle joints, and f) stride width (distance between feet during the double stance phase).

Using a semi-automated Matlab-based tracking software [32], several points of interest were encoded. The leg joints as well as the eye and the tail were tracked. The position of these reference points was used for computational analysis using an in-house Matlab code for calculating different basic locomotion parameters (e.g. stick diagrams, velocity, joints trajectory, angles, range, and elevation), steps pattern, and degree of similarity (Haimson B et al. *in preparation*). Dunnett's test [33] was used to perform multiple comparisons of group means following One-way ANOVA. Circular statistics was used for analyses of angular data.

Force test

The muscle strength was evaluated using the measurement of the angle of the fall from a ladder with a gradually increasing-angle. This test was repeated for each chicken at least 3 times, and the average falling angle was calculated.

Analysis of Left-right phase

Stride duration was measured as the time from 'Right toe-off'/foot-off' to the next Right 'toe-off' (as a complete stride cycle for the right leg), and the 'half-cycle' duration as the time of Right-toe off to the time of Left toe off. the following formula was used to calculate the phase: ((LeftToeOff_1 - RightToeOff_1)/ (RightToeOff_2 – RightToeOff_1))*360.

Table 1: Stride velocity and left-right phase in control and TeTx manipulated chicks

Swing velocity and left-right phase were measured and calculated as described in the Materials and Methods. One-way ANOVA followed by Dunnett's multiple comparison test were performed in order to compare the mean swing velocity in experimental chickens with the control1, α=0.05. All the *TeTX*-manipulated chicks (black font) were significantly different from control1 (red font). The Watson and Williams F test of the phase data (circular ANOVA) were not statistically significant (See also Supplementary statistics).

chick	Ave. Swing velocity (cm/sec)	Mean left-right phase (°)	# of steps
TeTX1	46.78 ± 22.13	184.679 ± 33.003	113
TeTX2	62.24 ± 20.17	182.293 ± 32.01	63
TeTX3	48.06 ± 20.04	180.784 ± 31.064	69
TeTX4	57.24 ± 24.35	180.502 ± 36.291	59
TeTX5	36.66 ± 17.61	181.97 ± 35.787	93
Control 1 (GFP)	79.65 ± 37.77	182.369 ± 35.366	47

Table 2: Maximum stride width in control and TeTx manipulated chicks

Stride width was measured as described in Materials and Methods ~~section~~. One-way ANOVA followed by Dunnett's.

chick	maximum stride width (cm)	# of steps
TeTX1	5.11 ± 1.89	97
TeTX2	5.32 ± 1.38	36
TeTX3	4.5 ± 1.01	27
TeTX4	4.9 ± 1.16	49
TeTX5	5.82 ± 1.71	110
Control 3	4.15 ± 1.07	137
Control 4	4.32 ± 1.32	115

Table 3: Collapses, knee height and TMP angle ranges in control and TeTx manipulated chicks.

Analysis of the range between the highest and lowest point of knee height and the highest and lowest angle of the TMP joint in all steps before and after subtraction of collapsed steps. The analysis was done as described in the results section and Fig. 6B, C.

The means of Control1 and Control 2 were significantly different from the means of the TeTx manipulated chicks, and significantly different from one another. Watson and Williams F test followed by pairwise comparison of means. (See also Supplementary statistics).

chick	% of steps with collapse	Knee Height. Average of range		TMP angle. Mean range(°)		# of steps
		All steps	Minus collapses	All steps	Minus collapses	
TeTX1	4.4	3.05 ± 0.49	2.87±0.38	82.27 ± 22	79.4±24.5	113
TeTX2	20.60	3.5 ± 0.3	3.35±0.47	71.79 ± 25	71.1±25.68	63
TeTX3	18.8	2.57 ± 0.31	2.27±0.26	64.17 ± 21	62.79±20.9	69
TeTX4	20.45	2.54 ± 0.55	2.477±0.56	72.48 ± 17	66.22±19.1	59
TeTX5	29	3.86 ± 0.83	3.2±0.2	72.86 ± 12	65.85±13.13	93
Control 1 (GFP)	2.12	1.91 ± 0.22	1.91±0.22	56.8 ± 16.6	56.8±16.6	47
Control 2 (GFP)	0	1.83 ± 0.25	1.83±0.25	41.42 ± 18.7	41.42 ± 18.7	20

Table 4: Correlations between joint angles and heights.

Angle to angle correlation coefficient is tested using Fisher's method 1993 [34], and the significance of the correlation is tested using the jackknife method [35]. Anglular to linear correlation is calculated according to Fisher 1993, Zar 1999 and the significance of the correlation is tested using the approximation of F distribution according to Mardia and Jupp

[36]. Correlation between linear variables is tested using Pearson Correlation. (See also Fig S8B and Supplementary statistics).

Parameters		Control1	Control2	TeTX1	TeTX2	TeTX3	TeTX4	TeTX5
TMP height	TMP angle	0.837	0.799	0.697	0.504	0.625	0.586	0.295
Ankle angle	TMP angle	-0.901	-0.868	-0.857	-0.818	-0.871	-0.875	-0.827
Ankle angle	TMP height	0.78	0.728	0.534	0.401	0.622	0.525	0.285

References

1 Brown, A. G. *Organization in the Spinal Cord: the Anatomy and Physiology of Identified Neurones*. (Springer, 1981).

2 Jankowska, E. & Hammar, I. Interactions between spinal interneurons and ventral spinocerebellar tract neurons. *J Physiol* **591**, 5445-5451, doi:10.1113/jphysiol.2012.248740 (2013).

3 Spanne, A. & Jorntell, H. Processing of multi-dimensional sensorimotor information in the spinal and cerebellar neuronal circuitry: a new hypothesis. *PLoS Comput Biol* **9**, e1002979, doi:10.1371/journal.pcbi.1002979 (2013).

4 Stecina, K., Fedirchuk, B. & Hultborn, H. Information to cerebellum on spinal motor networks mediated by the dorsal spinocerebellar tract. *J Physiol* **591**, 5433-5443, doi:10.1113/jphysiol.2012.249110 (2013).

5 Jiang, J., Azim, E., Ekerot, C. F. & Alstermark, B. Direct and indirect spino-cerebellar pathways: shared ideas but different functions in motor control. *Front Comput Neurosci* **9**, 75, doi:10.3389/fncom.2015.00075 (2015).

6 Bras, H., Cavallari, P. & Jankowska, E. Demonstration of initial axon collaterals of cells of origin of the ventral spinocerebellar tract in the cat. *J Comp Neurol* **273**, 584-592, doi:10.1002/cne.902730412 (1988).

7 Oscarsson, O. Functional organization of the ventral spino-cerebellar tract in the cat. I. Electrophysiological identification of the tract. *Acta Physiol Scand* **38**, 145-165, doi:10.1111/j.1748-1716.1957.tb01379.x (1956).

8 Baek, M., Menon, V., Jessell, T. M., Hantman, A. W. & Dasen, J. S. Molecular Logic of Spinocerebellar Tract Neuron Diversity and Connectivity. *Cell Rep* **27**, 2620-2635 e2624, doi:10.1016/j.celrep.2019.04.113 (2019).

9 Arshavsky, Y. I., Gelfand, I. M., Orlovsky, G. N. & Pavlova, G. A. Messages conveyed by descending tracts during scratching in the cat. I. Activity of vestibulospinal neurons. *Brain Res* **159**, 99-110, doi:10.1016/0006-8993(78)90112-9 (1978).

10 Baldissera, F. & ten Bruggencate, G. Rubrospinal effects on ventral spinocerebellar tract neurones. *Acta Physiol Scand* **96**, 233-249, doi:10.1111/j.1748-1716.1976.tb10192.x (1976).

11 Hammar, I., Krutki, P., Drzymala-Celichowska, H., Nilsson, E. & Jankowska, E. A trans-spinal loop between neurones in the reticular formation and in the cerebellum. *J Physiol* **589**, 653-665, doi:10.1113/jphysiol.2010.201178 (2011).

12 Furue, M. *et al.* Spinocerebellar projections from the cervical and lumbosacral enlargements in the chicken spinal cord. *Brain Behav Evol* **76**, 271-278, doi:10.1159/000321910 (2010).

13 Furue, M. *et al.* Trajectories in the spinal cord and the mediolateral spread in the cerebellar cortex of spinocerebellar fibers from the unilateral lumbosacral

enlargement in the chicken. *Brain Behav Evol* **77**, 45-54, doi:10.1159/000323380 (2011).

14 Uehara, M., Akita, M., Furue, M., Shinozaki, A. & Hosaka, Y. Z. Laterality of spinocerebellar neurons in the chicken spinal cord. *J Vet Med Sci* **74**, 495-498, doi:10.1292/jvms.11-0398 (2012).

15 Sakai, N., Insolera, R., Sillitoe, R. V., Shi, S.-H. & Kaprielian, Z. Axon sorting within the spinal cord marginal zone via Robo-mediated inhibition of N-cadherin controls spinocerebellar tract formation. *The Journal of neuroscience : the official journal of the Society for Neuroscience* **32**, 15377-15387 (2012).

16 Grillner, S. & El Manira, A. Current Principles of Motor Control, with Special Reference to Vertebrate Locomotion. *Physiol Rev* **100**, 271-320, doi:10.1152/physrev.00015.2019 (2020).

17 Lai, H. C., Seal, R. P. & Johnson, J. E. Making sense out of spinal cord somatosensory development. *Development* **143**, 3434-3448, doi:10.1242/dev.139592 (2016).

18 Osseward, P. J., 2nd & Pfaff, S. L. Cell type and circuit modules in the spinal cord. *Curr Opin Neurobiol* **56**, 175-184, doi:10.1016/j.conb.2019.03.003 (2019).

19 Alaynick, W. A., Jessell, T. M. & Pfaff, S. L. SnapShot: spinal cord development. *Cell* **146**, 178-178 e171, doi:10.1016/j.cell.2011.06.038 (2011).

20 Hadas, Y. *et al.* A 'tool box' for deciphering neuronal circuits in the developing chick spinal cord. *Nucleic Acids Res* **42**, e148, doi:10.1093/nar/gku750 (2014).

21 Morikawa, Y., Hisaoka, T. & Senba, E. Characterization of Foxp2-expressing cells in the developing spinal cord. *Neuroscience* **162**, 1150-1162, doi:10.1016/j.neuroscience.2009.05.022 (2009).

22 Francius, C. *et al.* Identification of multiple subsets of ventral interneurons and differential distribution along the rostrocaudal axis of the developing spinal cord. *PLoS One* **8**, e70325, doi:10.1371/journal.pone.0070325 (2013).

23 Avraham, O. *et al.* Transcriptional control of axonal guidance and sorting in dorsal interneurons by the Lim-HD proteins Lhx9 and Lhx1. *Neural Dev* **4**, 21, doi:1749-8104-4-21 [pii] 10.1186/1749-8104-4-21 (2009).

24 Delile, J. *et al.* Single cell transcriptomics reveals spatial and temporal dynamics of gene expression in the developing mouse spinal cord. *Development* **146**, doi:10.1242/dev.173807 (2019).

25 Bikoff, J. B. *et al.* Spinal Inhibitory Interneuron Diversity Delineates Variant Motor Microcircuits. *Cell* **165**, 207-219, doi:10.1016/j.cell.2016.01.027 (2016).

26 Cheng, L. *et al.* Tlx3 and Tlx1 are post-mitotic selector genes determining glutamatergic over GABAergic cell fates. *Nat Neurosci* **7**, 510-517, doi:10.1038/nn1221 (2004).

27 Gosgnach, S. *et al.* V1 spinal neurons regulate the speed of vertebrate locomotor outputs. *Nature* **440**, 215-219 (2006).

28 Griener, A., Zhang, W., Kao, H., Wagner, C. & Gosgnach, S. Probing diversity within subpopulations of locomotor-related V0 interneurons. *Dev Neurobiol* **75**, 1189-1203, doi:10.1002/dneu.22277 (2015).

29 Valenzuela, J. I., Hasan, S. J. & Steeves, J. D. Stimulation of the brainstem reticular formation evokes locomotor activity in embryonic chicken (in ovo). *Brain Res Dev Brain Res* **56**, 13-18, doi:10.1016/0165-3806(90)90158-u (1990).

30 Ruder, L., Takeoka, A. & Arber, S. Long-Distance Descending Spinal Neurons Ensure Quadrupedal Locomotor Stability. *Neuron* **92**, 1063-1078, doi:10.1016/j.neuron.2016.10.032 (2016).

31 Murray, A. J., Croce, K., Belton, T., Akay, T. & Jessell, T. M. Balance Control Mediated by Vestibular Circuits Directing Limb Extension or Antagonist Muscle Co-activation. *Cell Rep* **22**, 1325-1338, doi:10.1016/j.celrep.2018.01.009 (2018).

32 Hedrick, T. L. Software techniques for two- and three-dimensional kinematic measurements of biological and biomimetic systems. *Bioinspir Biomim* **3**, 034001, doi:10.1088/1748-3182/3/3/034001 (2008).

33 Dunnett, C. W. A Multiple Comparison Procedure for Comparing Several Treatments with a Control. *Journal of the American Statistical Association* **50**, 1096-1121 (1955).

34 Fisher, N. I. *Statistical Analysis of Circular Data*. (Cambridge University Press, 1993).

35 Zar, J. *Biostatistical Analysis, 4th Edition*. (Upper Saddle River, NJ: Prentice Hall, 1999).

36 Marida, K. V. & Jupp, P. E. *Directional Statistics*. (Wiley, 2000).

Fig. 1

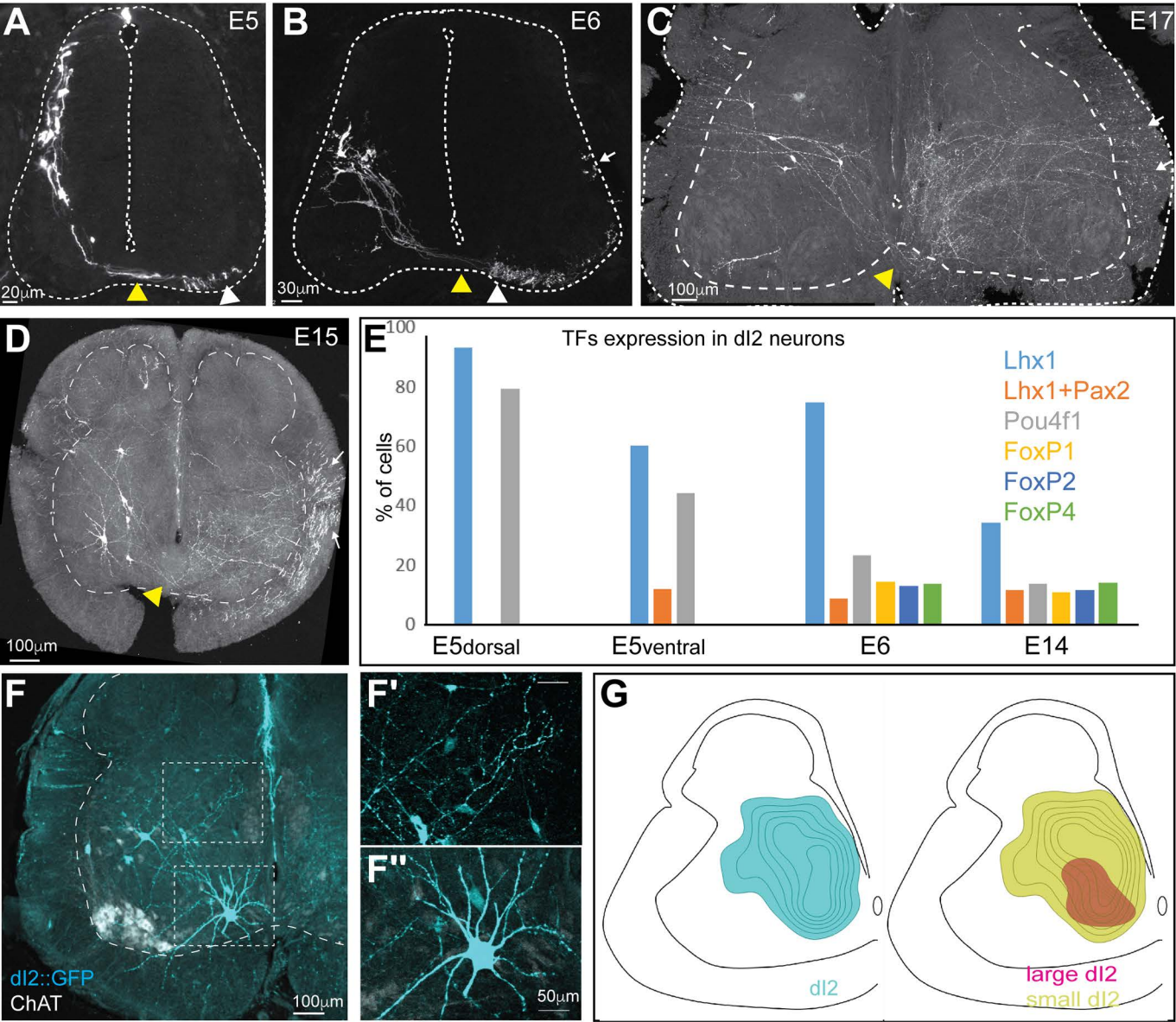
A
E5
20µm
B
E6
30µm
C
E17
100µm
D
E15
100µm
E
TFs expression in dI2 neurons
% of cells
100
80
60
40
20
0
Lhx1
Lhx1+Pax2
Pou4f1
FoxP1
FoxP2
FoxP4
E5dorsal
E5ventral
E6
E14
F
dI2::GFP
ChAT
100µm
F'
F''
50µm
G
dI2
large dI2
small dI2

Fig. 2

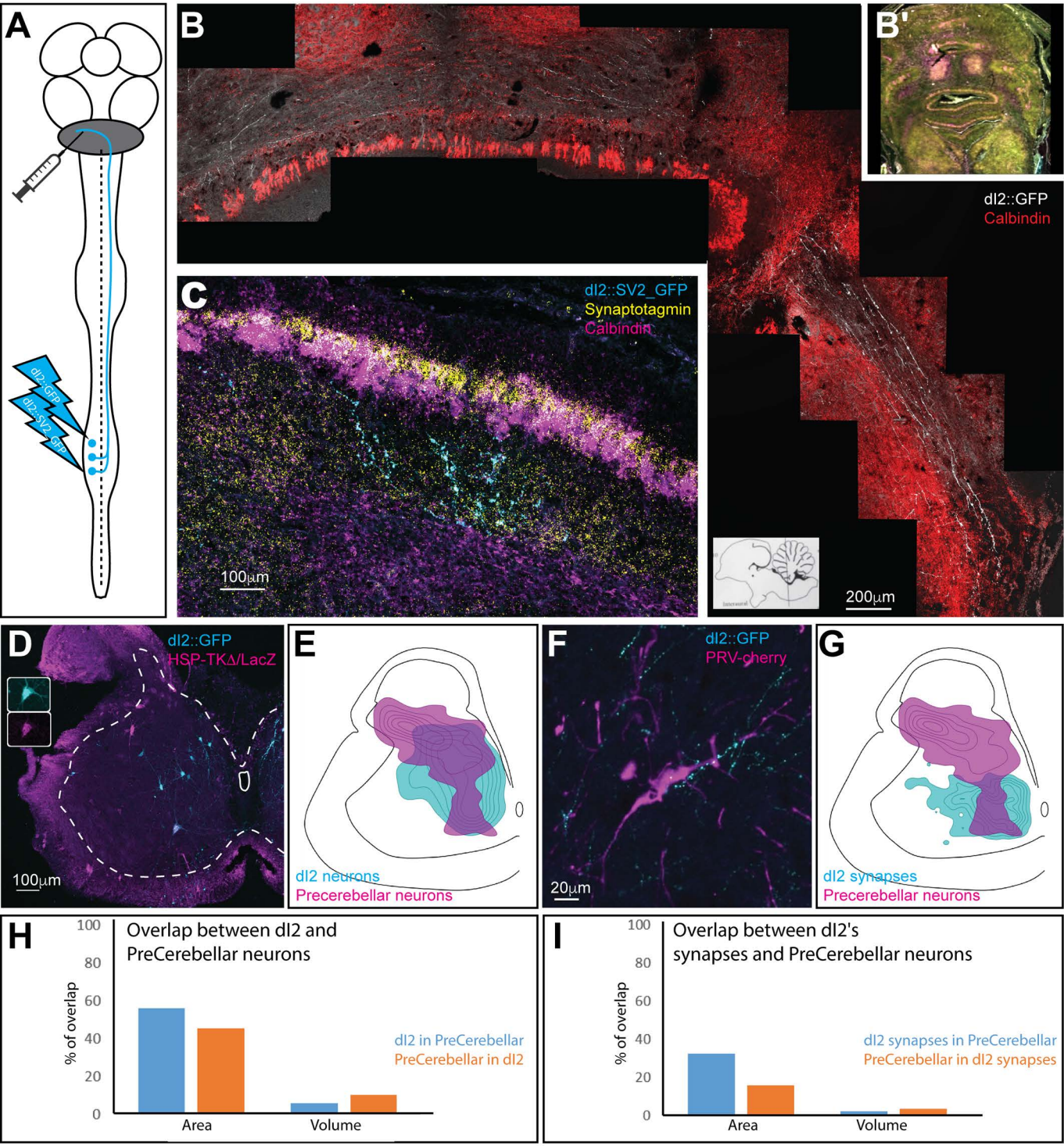
A
dI2::GFP
dI2::SV2_GFP
B
dI2::GFP
Calbindin
200µm
B'
C
dI2::SV2_GFP
Synaptotagmin
Calbindin
100µm
D
dI2::GFP
HSP-TKΔ/LacZ
100µm
E
dI2 neurons
Precerebellar neurons
F
dI2::GFP
PRV-cherry
20µm
G
dI2 synapses
Precerebellar neurons
H
Overlap between dI2 and PreCerebellar neurons
% of overlap
100
80
60
40
20
0
dI2 in PreCerebellar
PreCerebellar in dI2
Area
Volume
I
Overlap between dI2's synapses and PreCerebellar neurons
% of overlap
100
80
60
40
20
0
dI2 synapses in PreCerebellar
PreCerebellar in dI2 synapses
Area
Volume

Fig. 3

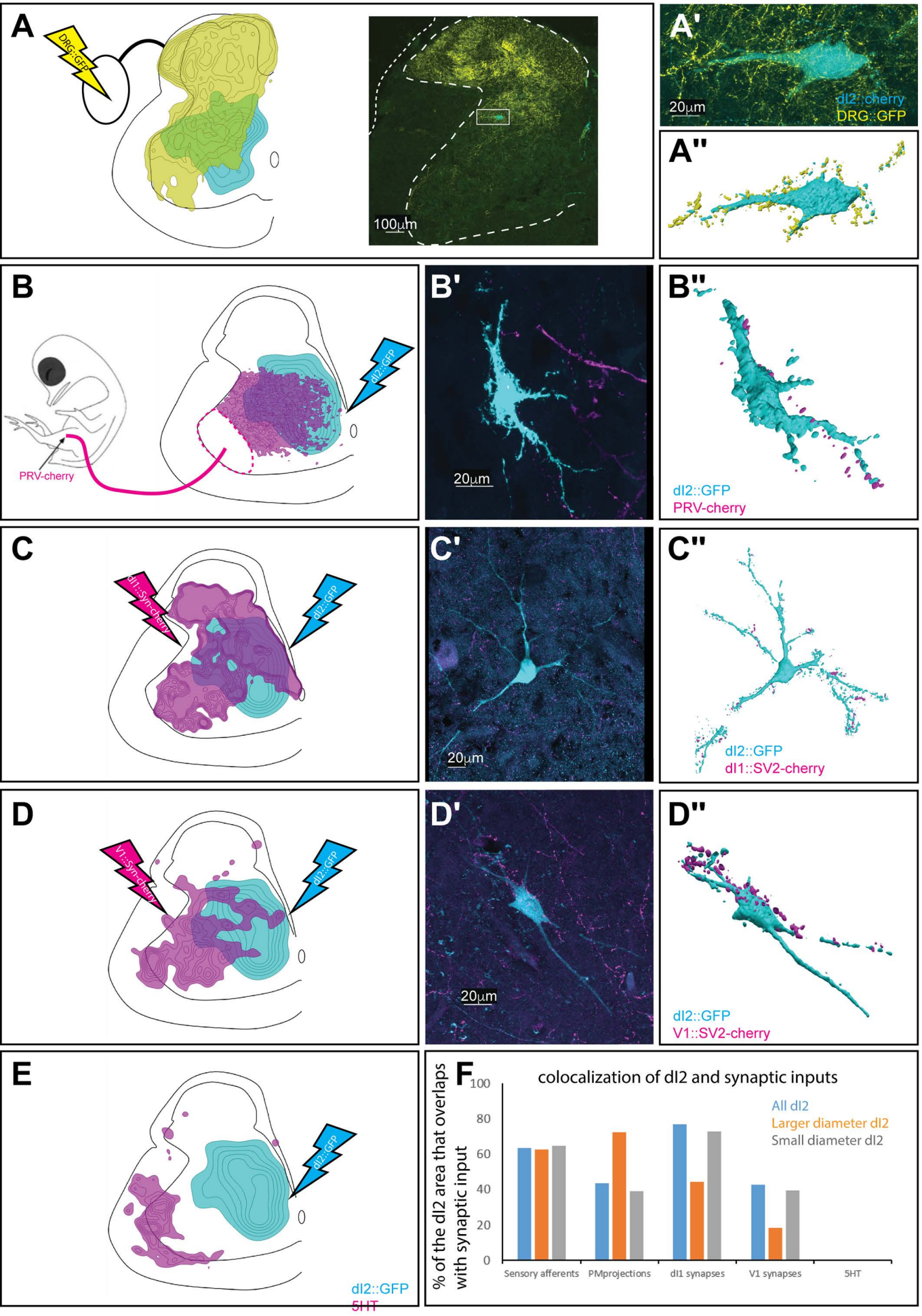
A
DRG::GFP
100μm
A'
20μm
dI2::cherry
DRG::GFP
A''
B
dI2::GFP
PRV-cherry
B'
20μm
B''
dI2::GFP
PRV-cherry
C
dI1::Syn-cherry
dI2::GFP
C'
20μm
C''
dI2::GFP
dI1::SV2-cherry
D
V1::Syn-cherry
dI2::GFP
D'
20μm
D''
dI2::GFP
V1::SV2-cherry
E
dI2::GFP
5HT
F
colocalization of dI2 and synaptic inputs
% of the dI2 area that overlaps with synaptic input
100
80
60
40
20
0
All dI2
Larger diameter dI2
Small diameter dI2
Sensory afferents
PMprojections
dI1 synapses
V1 synapses
5HT

Fig. 4

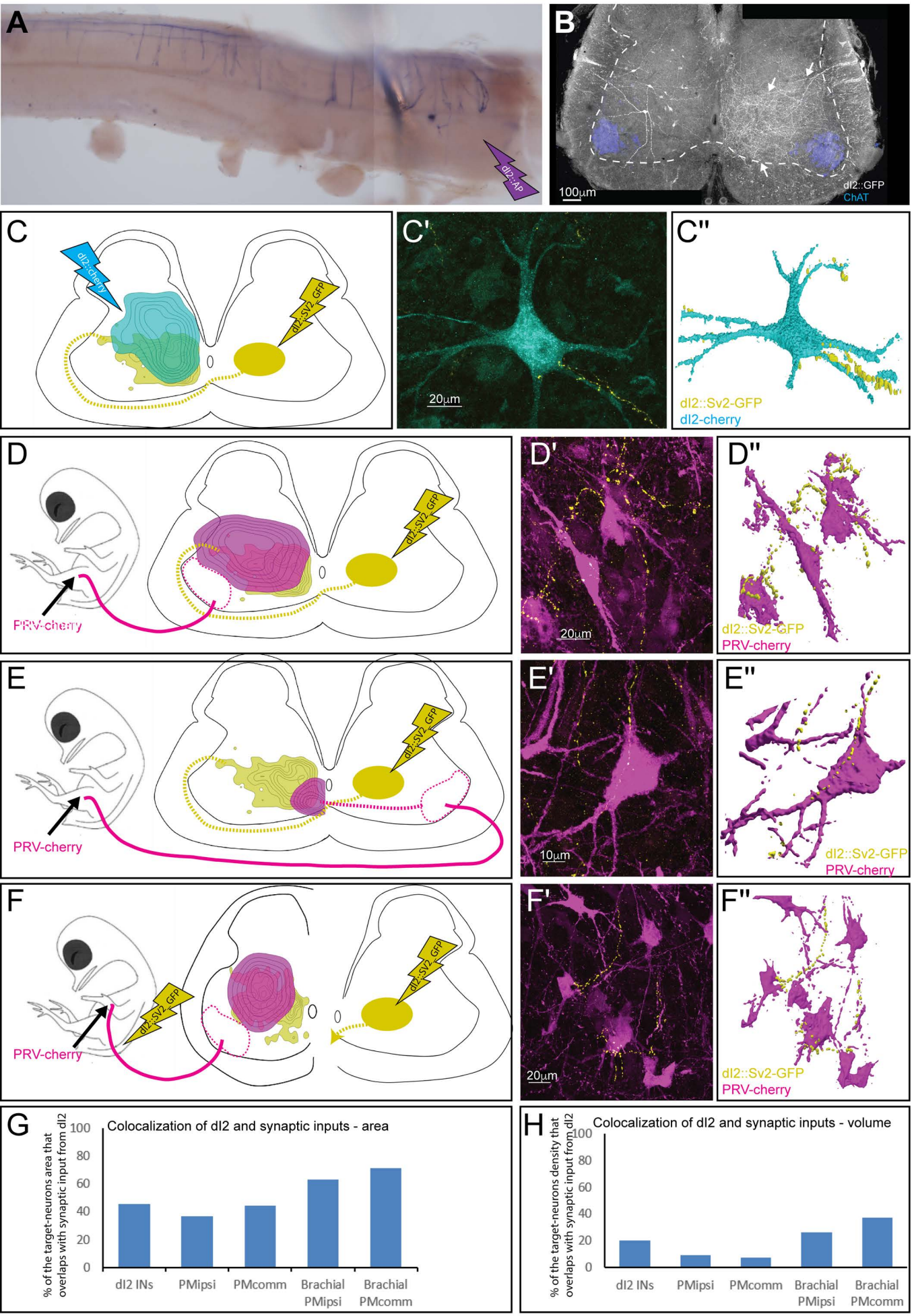
A
dI2::AP
B
100µm
dI2::GFP
ChAT
C
dI2::cherry
dI2::Sv2 GFP
C'
20µm
C''
dI2::Sv2-GFP
dI2-cherry
D
PRV-cherry
dI2::Sv2 GFP
D'
20µm
D''
dI2::Sv2-GFP
PRV-cherry
E
PRV-cherry
dI2::Sv2 GFP
E'
10µm
E''
dI2::Sv2-GFP
PRV-cherry
F
PRV-cherry
dI2::Sv2 GFP
dI2::Sv2 GFP
F'
20µm
F''
dI2::Sv2-GFP
PRV-cherry
G
Colocalization of dI2 and synaptic inputs - area
% of the target-neurons area that overlaps with synaptic input from dI2
100
80
60
40
20
0
dI2 INs
PMipsi
PMcomm
Brachial PMipsi
Brachial PMcomm
H
Colocalization of dI2 and synaptic inputs - volume
% of the target-neurons density that overlaps with synaptic input from dI2
100
80
60
40
20
0
dI2 INs
PMipsi
PMcomm
Brachial PMipsi
Brachial PMcomm

Fig. 5

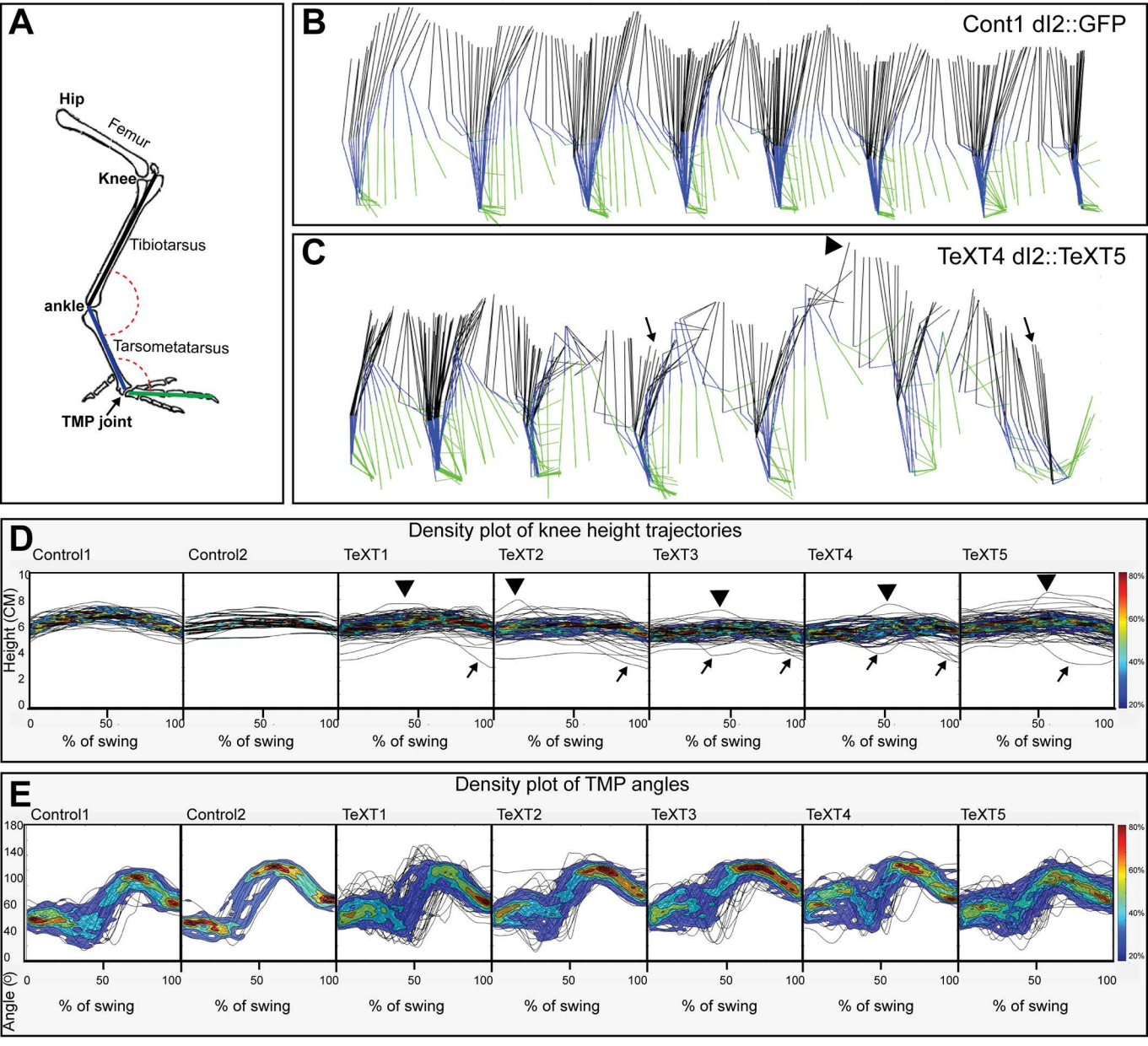
A
Hip
Femur
Knee
Tibiotarsus
ankle
Tarsometatarsus
TMP joint
B
Cont1 dl2::GFP
C
TeXT4 dl2::TeXT5
D
Density plot of knee height trajectories
Control1
Control2
TeXT1
TeXT2
TeXT3
TeXT4
TeXT5
Height (CM)
% of swing
80%
60%
40%
20%
E
Density plot of TMP angles
Angle (°)
% of swing

Fig. 6

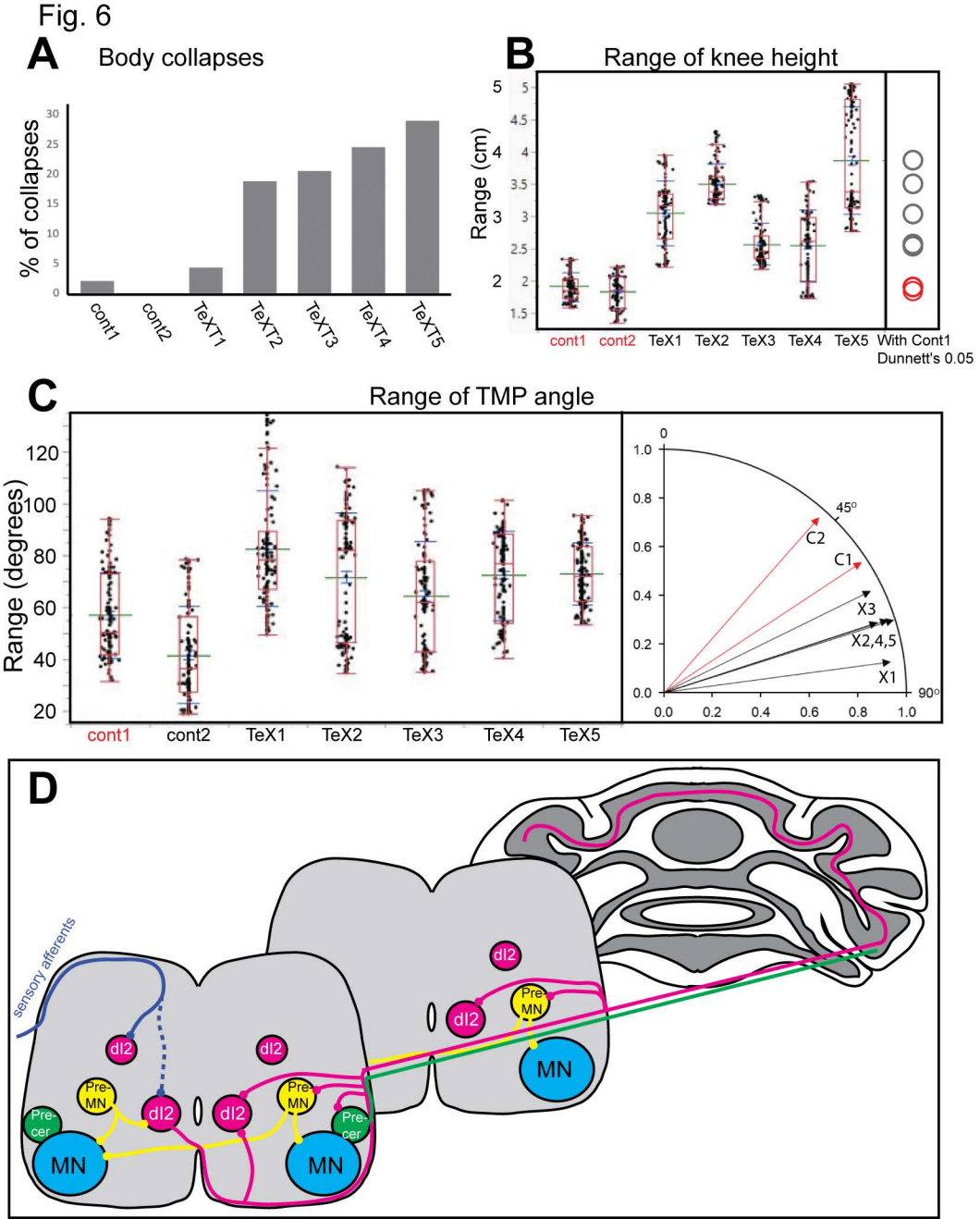
A
Body collapses
% of collapses
cont1
cont2
TeXT1
TeXT2
TeXT3
TeXT4
TeXT5
B
Range of knee height
Range (cm)
cont1
cont2
TeX1
TeX2
TeX3
TeX4
TeX5
With Cont1
Dunnett's 0.05
C
Range of TMP angle
Range (degrees)
cont1
cont2
TeX1
TeX2
TeX3
TeX4
TeX5
0
45°
90°
C2
C1
X3
X2,4,5
X1
D
sensory afferents
dI2
Pre-MN
Pre-cer
MN

A subpopulation of spinocerebellar tract neurons regulates the stability of bipedal stepping

Supplementary information

Supplementary Figure legends

Figure S1: Targeting, reporters, and activity modifiers, used in the study.

A. The different DNA constructs used in this study. For targeting expression in dI1 the EdI1 enhancer was used. For targeting dI2, intersection between *Ngn1* and *Foxd3* enhancers was attained. An Isl1 enhancer was used for targeting expression in DRG neuron [1]. **B.** A table summarizing the axonal projection, neurotransmitter identity, soma location, and the existence of synaptic connections between pre-MNs and spinal interneuron populations. Based on previous studies [2-4].

Figure S2: Differential expression of transcription factors in dI2 neurons.

A. Pre-migratory dI2 neurons are Lhx1^{+}Pax2^{-} (arrows). Cross section of the chick E5 neural tube, expressing GFP in dI2 neurons and immunostained for Lhx1 (yellow arrows) and Pax2.

B. Pre-migratory dI2 neurons express *FoxD3* (red arrow), and downregulate its expression upon ventral migration (yellow arrows). Cross section of a chick neural tube at E5, double labeled for dI2 dI2::GFP) and processed for *in situ* hybridization for *FoxD3* probe.

C. Genetic heterogeneity in dI2 neuron population. Only a small subset of dI2 neurons expresses the genes *FoxP2* and *FoxP4*. The arrow indicates a *FoxP2*$^{+}$/*FoxP4*$^{+}$ dI2::GFP neuron. Cross section of chick E6 neural tube expressing GFP in dI2 INs and immunostained for FoxP2 and FoxP4.

D. A small fraction of dI2 neurons express Pax2, an indicator of inhibitory phenotype. Cross section of chick E6 neural tube expressing GFP in dI2 INs and immunostained for Lhx1 and Pax2. The arrow points to a dI2::GFP/Lhx1^{+}/Pax2^{+} neuron.

Fig. S3: dI2s neurotransmitter phenotype and soma localization.

A-D. Most of dI2 neurons are excitatory. dI2 neurons expressing GFP together with *in situ* hybridization using the *Vglut2* probe (A) or the *GAD1* probe (C), and the corresponding quantification of the double-labeled neurons (B and D, respectively).

E. Density plot of dI2 soma in the crural plexus segments (*N*=551 cells) (left). Density plot of $dI2_{large}$ (magenta) and $dI2_{small}$ (yellow) neurons in the crural plexus segments (*N*=48 and *N*=502 cells, respectively) (right).

F. Density plot of dI2 soma in the brachial segments (*N*=66 cells)

Figure S4: dI2s densities at the crural plexus level and innervation of deep cerebellar nuclei.

A. dI2 synapses in the deep cerebellar nuclei. A cross section of chick E17 cerebellum. dI2 synapses (magenta), synaptotagmin (cyan). **B.** Density plot of dI2 and precerebellar neurons at the crural plexus segments (*N*=551 and *N*=652 cells, respectively). **C.** Quantification of the overlap in area and volume of the two density plots. **D.** Density plot of dI2 synapses and precerebellar neurons at the crural plexus segments (*N*=2543 synapses with density values 25-80% and *N*=652 cells with density values 10-90%, respectively). **E.** Quantification of the overlap in area and volume of the two density plots.

Figure S5: dI1i are pre-motoneurons

A, B. Schematic illustration of the strategy for studying the potential innervation of motor neurons by dI1 neurons (A). dI1 neurons were targeted by dI1 specific enhancer (Fig. S1A). At E15 synaptic boutons, labeled with SV2-GFP, were studied on cross sections. Synaptic reporter (cyan) was expressed in dI1 neurons. dI1i boutons contacting $Chat^+$ motorneurons (magenta) are apparent (B).

C, D. Schematic representation of the experimental design for co-labeling dI1 and pre-motoneurons, supplemented by cell soma densities of dI1 neurons (cyan, *N*=643 cells) and

pre-motoneurons (magenta, N=936 cells). dI1 neurons were labeled at HH18. At E13, PRV virus was injected to the leg musculature, and the embryo was incubated until infection of pre-motoneurons (35 hours) (C). In cross section of E13, PRV-cherry (magenta) is detected in motor neurons (Chat$^+$, yellow) and pre-motoneurons (D). An example of dI1 neurons co-expressing GFP and PRV-cherry shown in D'.

Figure S6: Input of 5HT and dI1 to dI2 neurons at the level of the crural plexus

A, B. Sparse sensory innervation on ventrally located dI2 neurons. Cross section of an E17 embryo at the lumbar spinal cord (crural plexus level). A ventrally located dI2 neuron is sparsely contacted by sensory afferents (A), magnified in B. **C, D.** Density plots of $dI2_{large}$ (magenta, *N*=48) and $dI2_{small}$ (yellow, *N*=502) neurons and sensory afferents (*N*=18 sections, with density values 10-80%) in the crural plexus segments. **E.** dI1 neurons form synapses on dI2 neurons (*N*=13369 synapses with density values 50-90%). Example of dI1 boutons (magenta) on a dI2 neuron (cyan) (E') and its 3D reconstruction in (E'').

F. dI2 are not contacted by 5HT synaptic terminals (*N*=2754 synapses with density values 25-85%). E17 cross sections of dI2::GFP labeled embryos were stained for 5HT.

G. Quantification of the overlap in volume of the different input sources and dI2 neurons densities plots.

Figure S7: Spinal targets of dI2

Schematic representations of the experimental design for labelling synapses (dI2::SV2-GFP, yellow) and potential targets (magenta or cyan), supplemented by cell soma density. The targets and the dI2's synaptic densities are illustrated in A, B, C and E. Examples of target neurons contacted dI2's synaptic boutons are presented in A', B', C' and E'; and their 3D reconstruction in A'', B', C'' and E''. Genetic labelling was attained using dI2 enhancers (Supp

Fig. S1) electroporated at HH18. Pre-MNs were labelled by injection of PRV-cherry into the hindlimbs (D, E) or the forelimb (F) musculature, at E13. Embryo was incubated until pre-motorneurons infection (39 hours).

A. dI2 innervate ipsilateral projecting pre-motoneurons at the crural plexus level (*N*=2543 synapses and *N*=250 cells, respectively).

B. dI2 innervate contralateral projecting pre-motoneurons at the crural plexus level (*N*=2543 synapses and *N*=117 cells, respectively).

C. dI2 innervate the contralateral dI2 neurons at the crural plexus level (*N*=2543 synapses and *N*=551 cells, respectively).

D. dI2 innervate brachial contralateral projecting pre-MNs (*N*=2215 synapses and *N*=90 cells, respectively).

E. dI2 innervate brachial dI2 neurons (N=2215 synapses and *N*=66 cells, respectively).

F. Quantification of the overlap in area and volume of the different synaptic targets and dI2 synapse density plots, as percentage of overlap of dI2 synapses with the target.

Figure S8: Locomotion characteristics of control and *TeTX*-treated chicks.

A. The mean left-right phase of the control and *TeTX*-treated chicks. The mean phase values are pointed at by the r-vectors (arrows). The Rayleigh critical values (P=0.05) are indicated by blue circles.

B. Correlation scatter plot matrices of the height vs. angle of the TMP joint, the ankle angle vs. TMP height, and the TMP angle vs. the ankle angle during the last 26 epochs (20.6%) of the swing phase in the control and the TeTx manipulated chicks. Angle values are in degrees, heights in cm. The 95% confidence ellipses are shown in red.

Supplementary tables

S1: Weight, force and number of electroporated cells

chick	# of dI2::TeTX cells	% of large diameter dI2::TeTX cells	Weight in gr.	Force test % of fall	
				Mean ± circ*SD*	*N*
TeTX1	602	5.64	139	68.41 ± 2.8	3
TeTX2	124	6.45	139	63.34 ± 1.85	3
TeTX3	81	7.4	159	65.45 ± 3.35	5
TeTX4	755	7.01	148	69.29 ± 3.48	5
TeTX5	769	8.71	139	66.44 ± 3.75	3
Control 5			144	66.93 ± 3.59	6
Control 6			135	64.61 ± 2.57	6
Control 7			122	66.11 ± 5.57	7

Supplementary Statistical analysis

Fig. 6A: Body Collapses

Z test results			
		Z score	p Value
Control1	Control2	0.6395	0.52218
Control1	TeTX1	-0.6932	0.4902
Control1	TeTX2	-2.8791	0.00398
Control1	TeTX3	-2.7099	0.00672
Control1	TeTX4	-3.2439	0.0012
Control1	TeTX5	-3.7566	0.00016
Control2	TeTX1	-0.9321	0.35238
Control2	TeTX2	-2.1564	0.03078
Control2	TeTX3	-2.0468	0.04036
Control2	TeTX4	-2.39	0.01684
Control2	TeTX5	-2.694	0.00714

Fig. 6B: Statistical analysis
Analysis of Range (Knee Height)

ANOVA results					
Source	SS	df	MS	F	prob>F
Groups	443.071	6	73.8452	329.98	9.50E-221
Error	195.816	875	0.2238		
Total	638.887	881			

Quantiles

Level	Minimum	10%	25%	Median	75%	90%	Maximum
Control1	1.583211	1.642068	1.732058	1.853918	2.036332	2.302025	2.338401
Control2	1.356529	1.505224	1.553307	1.852974	2.061026	2.171198	2.220186
TeXT1	2.221573	2.267482	2.648965	3.163871	3.358293	3.798085	3.948563
TeXT2	3.180134	3.230696	3.278528	3.375239	3.61459	4.067007	4.314338
TeXT3	2.190001	2.274949	2.343899	2.461626	2.703694	3.196665	3.322023
TeXT4	1.739098	1.764574	1.977728	2.614597	2.978234	3.317682	3.538927
TeXT5	2.771483	2.882091	3.133971	3.380367	4.820164	5.003136	5.048257

Means and Std Deviations

Level	Number	Mean	Std Dev	Std Err Mean	Lower 95%	Upper 95%
Control1	126	1.9145771	0.2262921	0.0201597	1.8746786	1.9544757
Control2	126	1.8364371	0.2550249	0.0227194	1.7914725	1.8814016
TeXT1	126	3.0513864	0.4980589	0.0443706	2.9635714	3.1392014
TeXT2	126	3.5073422	0.3048273	0.0271562	3.4535968	3.5610877
TeXT3	126	2.5748662	0.3189396	0.0284134	2.5186326	2.6310999
TeXT4	126	2.5439144	0.5507457	0.0490643	2.44681	2.6410188
TeXT5	126	3.8665367	0.8392009	0.074762	3.7185735	4.0144999

Means Comparisons
Comparisons with a control using Dunnett's Method
Control Group = 1Control1
Confidence Quantile

|d|	Alpha
2.57201	0.05

LSD Threshold Matrix

Level	Abs(Dif)-LSD	p-Value
TeXT5	1.799	<.0001*
TeXT2	1.439	<.0001*
TeXT1	0.984	<.0001*
TeXT3	0.507	<.0001*
TeXT4	0.476	<.0001*
Control1	-0.15	1.0000
Control2	-0.08	0.6020

Positive values show pairs of means that are significantly different.

Fig. 6C: Statistical analysis
Analysis of Range (TMP Angle)

BASIC STATISTICS							
Variable	Control 1	Control 2	TeTX1	TeTX2	TeTX3	TeTX4	TeTX5
Data Type	Angles	Angles	Angles	Angles	Angles	Angles	Angles
Number of Observations	126	126	126	126	126	126	126
Mean Vector (μ)	56.804	41.427	82.279	71.793	64.171	72.488	72.866
Length of Mean Vector (r)	0.959	0.948	0.928	0.908	0.933	0.956	0.978
Circular Standard Deviation	16.583	18.673	22.21	25.234	21.269	17.213	12.024
One Sample Tests							
Rayleigh Test (Z)	115.875	113.304	108.421	103.784	109.78	115.126	120.571
Rayleigh Test (p)	< 1E-12	< 1E-12	< 1E-12	< 1E-12	< 1E-12	< 1E-12	< 1E-12

WATSON-WILLIAMS F-TESTS					
Variables (& observations)	F	p	df	df2	Est. Mean
Multi-sample test using:					
Control1 (126)					
Control2 (126)					
TeTX1 (126)					
TeTX2 (126)					
TeTX3 (126)					
TeTX4 (126)					
TeTX5 (126)	59.777	< 1E-12	6	875	65.993

WATSON-WILLIAMS F-TESTS					
Variables (& observations)	F	p	df	df2	Est. Mean
Control1 & Control2 (126 & 126)	47.787	3.94E-11	1	250	49.159
Control1 & TeTX1 (126 & 126)	106.55	< 1E-12	1	250	69.327
Control1 & TeTX2 (126 & 126)	31.286	5.83E-08	1	250	64.091
Control1 & TeTX3 (126 & 126)	9.436	0.002	1	250	60.438
Control1 & TeTX4 (126 & 126)	54.221	2.59E-12	1	250	64.634
Control1 & TeTX5 (126 & 126)	77.372	< 1E-12	1	250	64.915
Control2 & TeTX1 (126 & 126)	248.275	< 1E-12	1	250	61.618
Control2 & TeTX2 (126 & 126)	118.122	< 1E-12	1	250	56.269
Control2 & TeTX3 (126 & 126)	81.412	< 1E-12	1	250	52.708
Control2 & TeTX4 (126 & 126)	187.698	< 1E-12	1	250	57.021
Control2 & TeTX5 (126 & 126)	251.63	< 1E-12	1	250	57.397
TeTX1 & TeTX2 (126 & 126)	12.335	0.000527	1	250	77.094
TeTX1 & TeTX3 (126 & 126)	43.812	2.19E-10	1	250	73.197
TeTX1 & TeTX4 (126 & 126)	15.366	0.000114	1	250	77.31
TeTX1 & TeTX5 (126 & 126)	17.641	3.71E-05	1	250	77.447
TeTX2 & TeTX3 (126 & 126)	6.764	0.01	1	250	67.928
TeTX2 & TeTX4 (126 & 126)	0.066	0.798	1	250	72.15

TeTX2 & TeTX5 (126 & 126)	0.188	0.665	1	250	72.349
TeTX3 & TeTX4 (126 & 126)	11.685	0.000735	1	250	68.379
TeTX3 & TeTX5 (126 & 126)	16.057	8.11E-05	1	250	68.62
TeTX4 & TeTX5 (126 & 126)	0.041	0.84	1	250	72.679

Table S1: Force Test

BASIC STATISTICS								
Variable	Control5	Control6	Control7	TeTX1	TeTX2	TeTX3	TeTX4	TeTX5
Data Type	Angles	Angles	Angles	Angles	Angles	Angles	Angles	Angles
Number of Observations	6	6	7	3	3	5	5	3
Mean Vector (μ)	66.928	64.619	66.12	68.41	63.643	68.453	69.297	66.444
Length of Mean Vector (r)	0.998	0.999	0.995	0.999	1	0.999	0.999	0.999
Circular Standard Deviation	3.592	2.57	5.569	2.291	1.516	2.997	3.114	3.069
One Sample Tests								
Rayleigh Test (Z)	5.976	5.988	6.934	2.995	2.998	4.986	4.985	2.991
Rayleigh Test (p)	< 1E-12	< 1E-12	< 1E-12	0.034	0.033	0.001	0.001	0.034

WATSON-WILLIAMS F-TESTS					
Variables (& observations)	F	p	df	df2	Est. Mean
Multi-sample test using:					
Control1 (6)					
Control2 (6)					
Control3 (7)					
TeTX1 (3)					
TeTX2 (3)					
TeTX3 (5)					
TeTX4 (5)					
TeTX5 (3)	1.029	0.432	7	30	66.747

Table 1
Analysis of Swing Velocity By Chick

ANOVA results					
Source	SS	df	MS	F	prob>F
Groups	70166	5	14033.2	26.04	4.8E-23
Error	236009	438	538.8		
Total	306175	443			

Quantiles

Level	Minimum	10%	25%	Median	75%	90%	Maximum
Cont1	19.30492	32.64836	47.98796	76.92657	107.1323	126.5981	184.8968
TeTx1	12.01368	24.46136	28.23629	44.57757	58.86652	76.01989	118.7776
TeTx2	29.36873	32.47444	45.81093	64.43703	78.44142	86.82797	106.0823
TeTx3	8.832352	19.88817	37.42166	45.01577	61.24445	81.15453	88.9005
TeTx4	11.45893	22.89022	35.45376	59.75011	79.50531	87.37675	101.7187
TeTx5	10.53762	18.12198	23.07078	33.70597	47.79773	62.45216	97.50062

Means and Std Deviations

Level	Number	Mean	Std Dev	Std Err Mean	Lower 95%	Upper 95%
Cont1	47	79.651545	37.772865	5.5097387	68.561016	90.742073
TeTx1	113	46.78734	22.134462	2.0822351	42.661658	50.913022
TeTx2	63	62.241904	20.174634	2.541765	57.160988	67.322819
TeTx3	69	48.064883	20.041852	2.4127555	43.250304	52.879461
TeTx4	59	57.239154	24.353966	3.1706164	50.892475	63.585832
TeTx5	93	36.666793	17.617412	1.8268405	33.03853	40.295056

Means Comparisons
Comparisons with a control using Dunnett's Method
Control Group = GFP1
Confidence Quantile

|d|	Alpha
2.48137	0.05

LSD Threshold Matrix

Level	Abs(Dif)-LSD	p-Value
Cont1	-11.9	1.0000
TeTx2	6.308	0.0005*
TeTx4	11.15	<.0001*
TeTx3	20.69	<.0001*
TeTx1	22.87	<.0001*
TeTx5	32.68	<.0001*

Positive values show pairs of means that are significantly different.

Table 2: Statistical analysis
Comparison of maximum delta per stride

ANOVA results					
Source	SS	df	MS	F	prob>F
Groups	220.94	6	36.8233	17.58	1.05E-18
Error	1181.62	564	2.0951		
Total	1402.56	570			

Quantiles

Level	Minimum	10%	25%	Median	75%	90%	Maximum
Control3	1.367596	2.843941	3.388987	4.047114	4.895785	5.652417	6.379741
Control4	1.18938	2.550268	3.253339	4.307534	5.311383	5.995616	7.939445
TeTX1	0.34284	3.260252	3.817822	4.999565	6.136319	7.413171	11.8446
TeTX2	2.176949	3.825371	4.514134	5.429668	5.755859	6.651419	10.36888
TeTX3	1.613126	2.939709	4.042566	4.794431	4.957137	5.403267	6.341758
TeTX4	2.95143	3.469008	4.127639	5.111682	5.50772	5.921419	9.004741
TeTX5	1.642539	4.121106	4.789288	5.538087	6.422167	9.005017	10.24161

Means and Std Deviations

Level	Number	Mean	Std Dev	Std Err Mean	Lower 95%	Upper 95%
Control3	137	4.1500897	1.0749626	0.0918402	3.96847	4.3317093
Control4	115	4.3271494	1.321059	0.1231894	4.0831122	4.5711866
TeTX1	97	5.1120102	1.8971602	0.1926274	4.7296477	5.4943726
TeTX2	36	5.3208716	1.3849789	0.2308298	4.8522622	5.7894811
TeTX3	27	4.5069349	1.0170163	0.1957249	4.1046166	4.9092531
TeTX4	49	4.9071678	1.164942	0.1664203	4.5725574	5.2417782
TeTX5	110	5.8255975	1.7156012	0.1635762	5.5013949	6.1498002

Means Comparisons
Comparisons with a control using Dunnett's Method
Control Group = Control1
Confidence Quantile

|d|	Alpha
2.61488	0.05

LSD Threshold Matrix

Level	Abs(Dif)-LSD	p-Value
TeTX5	1.191	<.0001*
TeTX2	0.462	0.0001*
TeTX1	0.46	<.0001*
TeTX4	0.127	0.0102*
TeTX3	-0.44	0.7654
Control3	-0.3	0.8836
Control4	-0.46	1.0000

Positive values show pairs of means that are significantly different.

Table 1 and Fig. S8A: Phase analysis

BASIC STATISTICS							
Variable	GFP1	GFP2	TeTX1	TeTX2	TeTX3	TeTX4	TeTX5
Data Type	Angles	Angles	Angles	Angles	Angles	Angles	Angles
Number of Observations	75	31	204	155	114	79	142
Mean Vector (μ)	182.369	182.384	184.674	182.293	180.784	180.502	181.97
Length of Mean Vector (r)	0.827	0.897	0.847	0.856	0.863	0.818	0.823
Circular Standard Deviation	35.366	26.708	33.003	32.01	31.064	36.291	35.787
One Sample Tests							
Rayleigh Test (Z)	51.239	24.946	146.4	113.443	84.966	52.892	96.131
Rayleigh Test (p)	< 1E-12	7.34E-11	< 1E-12	< 1E-12	< 1E-12	< 1E-12	< 1E-12

WATSON-WILLIAMS F-TESTS					
Variables (& observations)	F	p	df	df2	Est. Mean
Multi-sample test using:					
GFP1 (75)					
GFP2 (31)					
TeTX1 (204)					
TeTX2 (155)					
TeTX3 (114)					
TeTX4 (79)					
TeTX5 (142)	0.25	0.959	6	793	182.466

Table 4, Fig. S8B: Correlation P-values

Parameters		Control1	Control2	TeTX1	TeTX2	TeTX3	TeTX4	TeTX5
TMP height	TMP angle	< 1E-12	< 1E-12	< 1E-12	< 1E-12	< 1E-12	< 1E-12	< 1E-12
Ankle angle	TMP angle	< 0.05	< 0.05	< 0.05	< 0.05	< 0.05	< 0.05	< 0.05
Ankle angle	TMP height	< 1E-12	< 1E-12	< 1E-12	< 1E-12	< 1E-12	< 1E-12	< 1E-12

Pairwise Comparisons using Z test (for TMP angle:Ankle angle it was preceded by Fisher r-to-z transformation)							
		TMP angle:Ankle angle		TMP Height:TMP angle		TMP Height:Ankle angle	
		Z	pvalue	Z	pvalue	Z	pvalue
Control1	Control2	-0.52	0.6031	0.3551	0.35942	0.4353	0.32997
Control1	TeTX1	-0.66	0.5093	1.1941	0.11702	1.8684	0.03074
Control1	TeTX2	-1.11	0.267	2.5544	0.00539	2.7789	0.00272
Control1	TeTX3	-0.48	0.6312	1.7237	0.04272	1.2443	0.10749
Control1	TeTX4	-0.42	0.6745	1.9975	0.02275	1.9308	0.0268
Control1	TeTX5	-1.01	0.3125	3.9429	0.00004	3.5771	0.00017
Control2	TeTX1	-0.15	0.8808	0.8471	0.19766	1.4496	0.07353
Control2	TeTX2	-0.59	0.5552	2.2322	0.01287	2.3779	0.00866
Control2	TeTX3	0.04	0.9681	1.3854	0.08226	0.816	0.20611
Control2	TeTX4	0.1	0.9203	1.6643	0.04846	1.5131	0.06552
Control2	TeTX5	-0.5	0.6171	3.6506	0.00013	3.1948	0.00071

Supplementary References

1 Uemura, O. *et al.* Comparative functional genomics revealed conservation and diversification of three enhancers of the isl1 gene for motor and sensory neuron-specific expression. *Dev Biol* **278**, 587-606, doi:10.1016/j.ydbio.2004.11.031 (2005).

2 Jessell, T. M. Neuronal specification in the spinal cord: inductive signals and transcriptional codes. *Nat Rev Genet* **1**, 20-29 (2000).

3 Alaynick, W. A., Jessell, T. M. & Pfaff, S. L. SnapShot: spinal cord development. *Cell* **146**, 178-178 e171, doi:10.1016/j.cell.2011.06.038 (2011).

4 Lai, H. C., Seal, R. P. & Johnson, J. E. Making sense out of spinal cord somatosensory development. *Development* **143**, 3434-3448, doi:10.1242/dev.139592 (2016).

Fig. S1

A

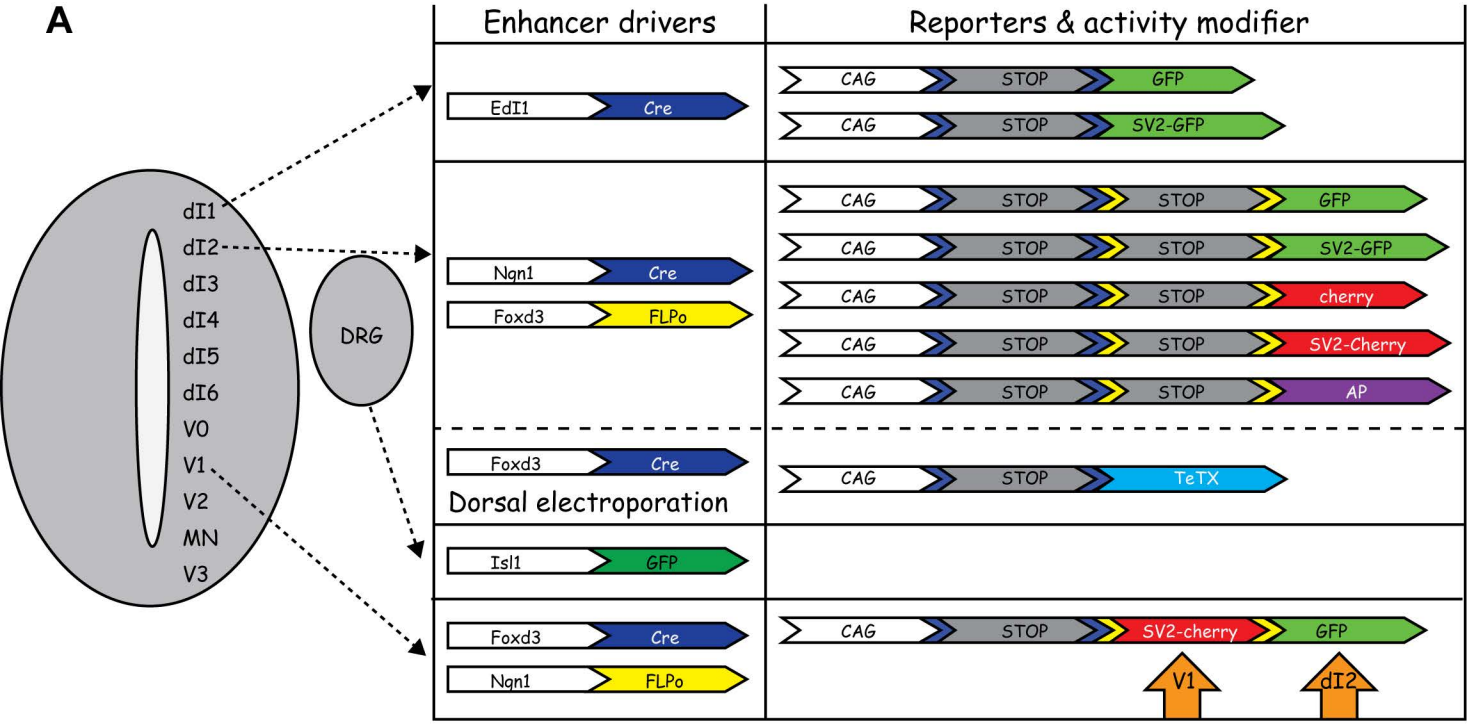

B

	Axonal projection	Neurotransmitter	Soma location	Pre-MN
dI1c	C	E	V	No
dI1i	I	E	M	Yes
dI2	C	E	M/V	No
dI3	I	E	D/M	Yes
dI4	I	I	D	No
dIL	I	E/I	D	
dI5	I	E	D	Yes
dI6	I/C	I	M/V	Yes
V0	C	I/E	M/V	Yes
V1	I	I	M/V	Yes
V2	I	E/I	M/V	Yes
V3	C	E	D	Yes

Fig. S2: Differential expression of TFs in dI2 INs.

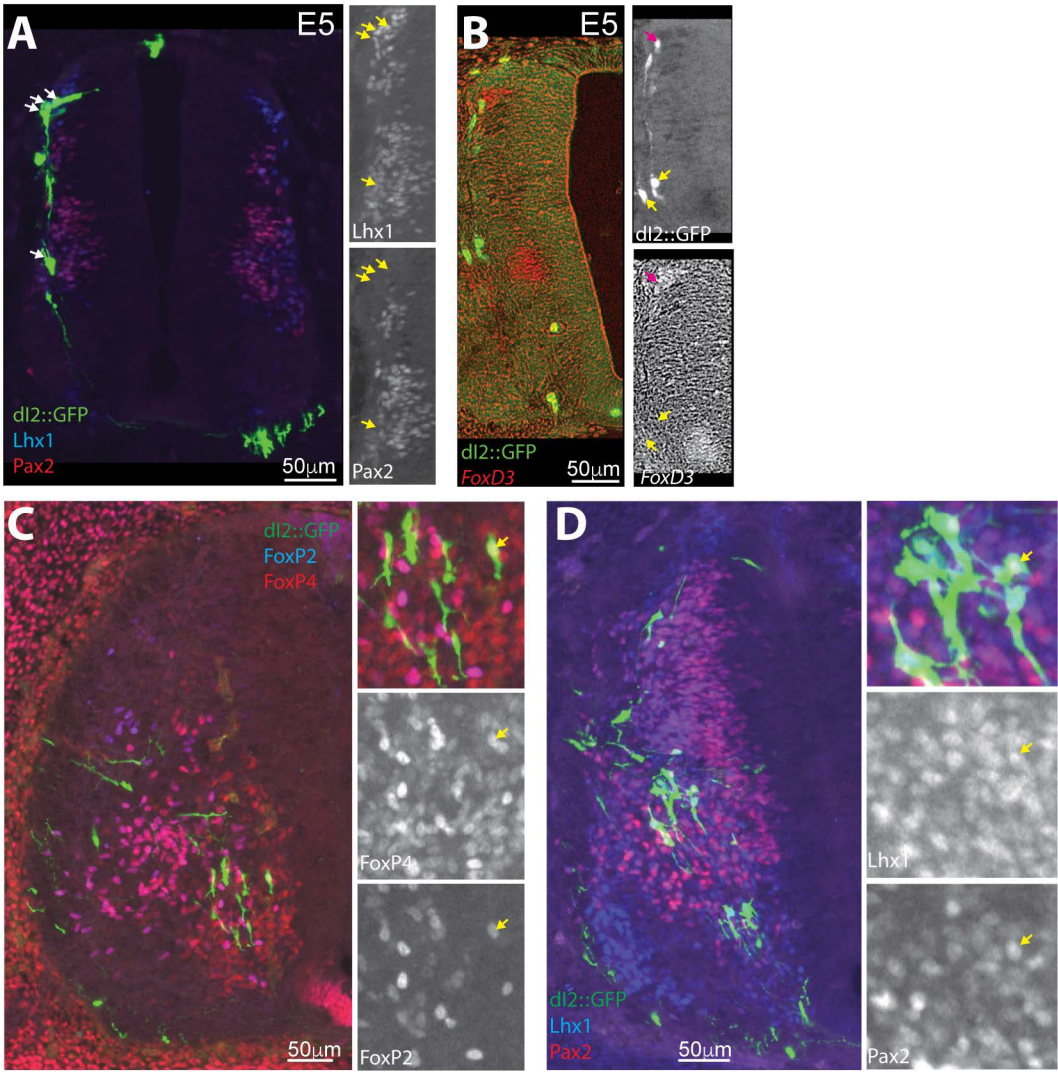

Fig. S3: dI2s Neuro-transmitter phenotype and soma localization.

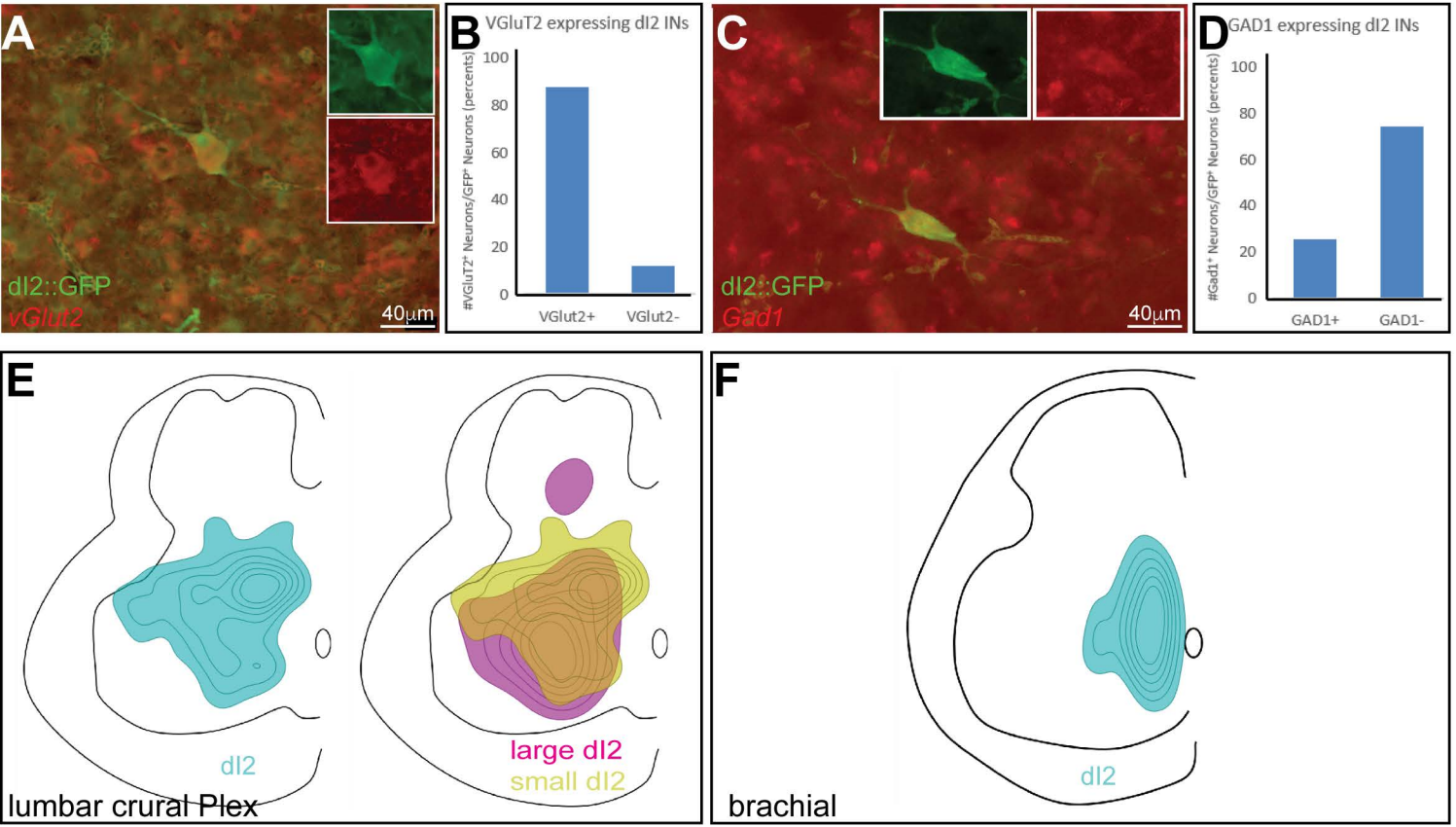

Fig. S4: dI2s densities at the crural plexus level and innervation of deep cerebellar nuclei.

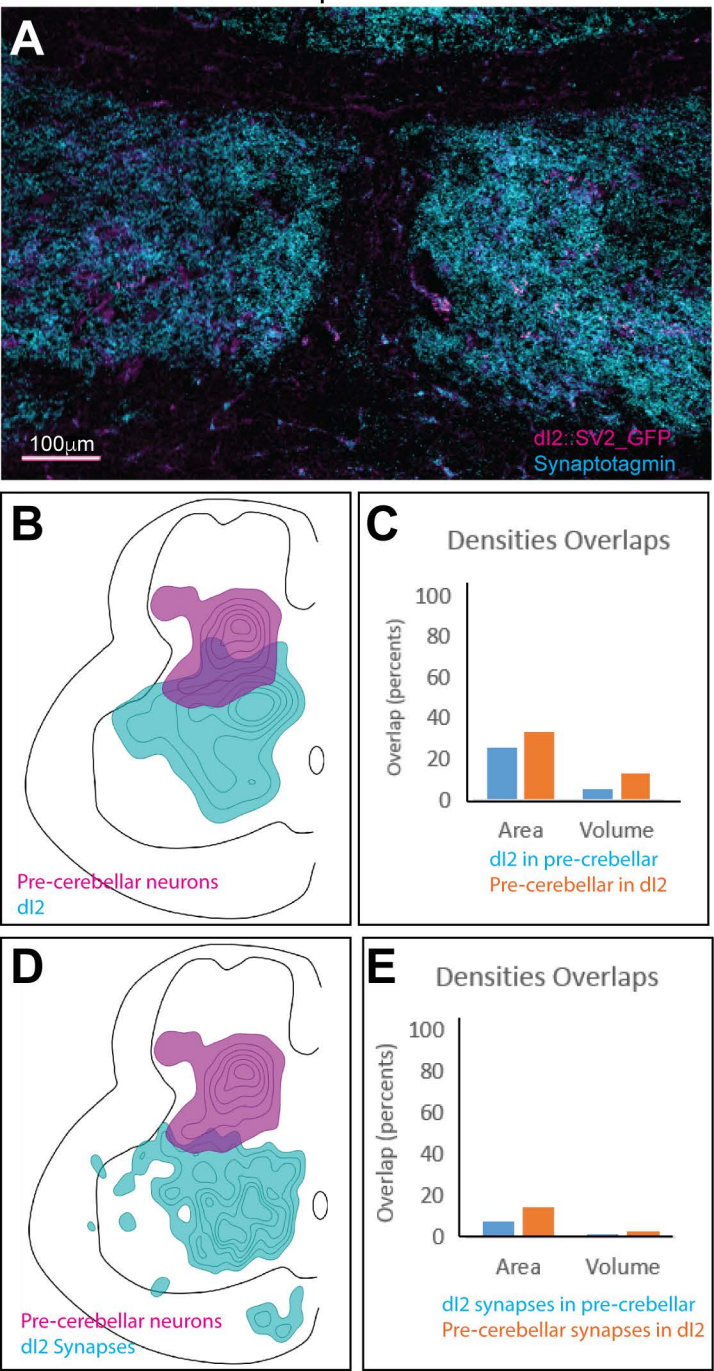

Fig. S5: dI1i are pre-MNs

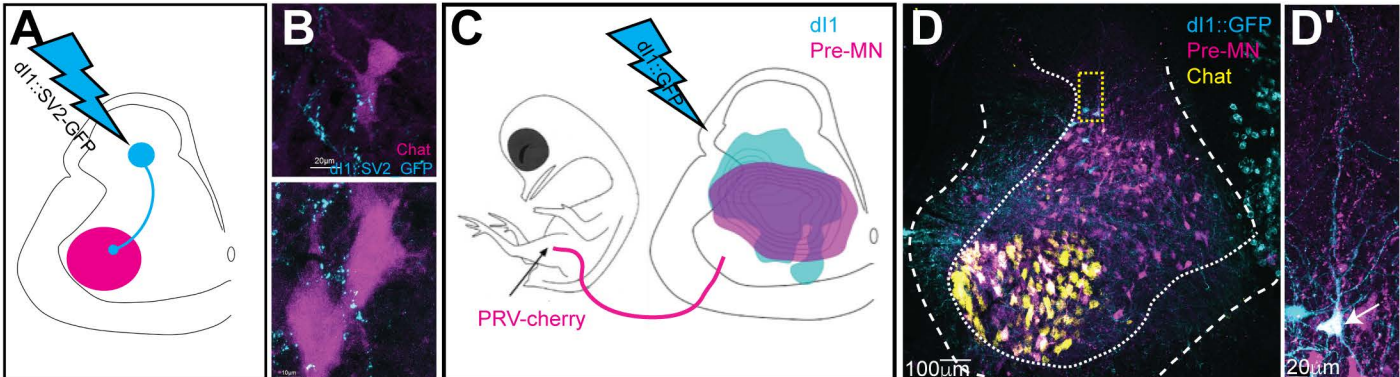

Fig. S6: Input of 5HT and dI1 to dI2 neurons at the level of the crural plexus

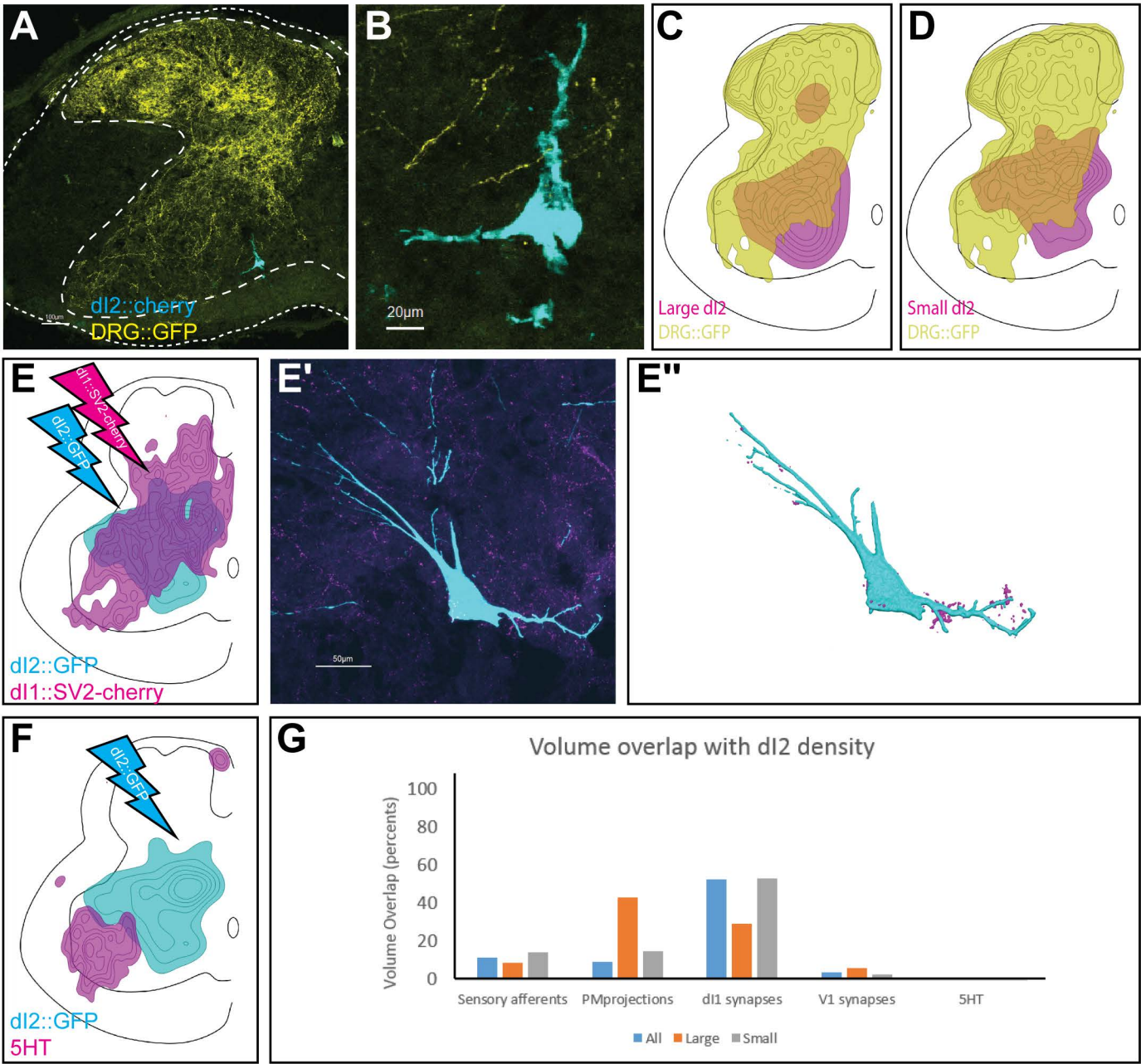

Fig. S7: Spinal targets of dI2

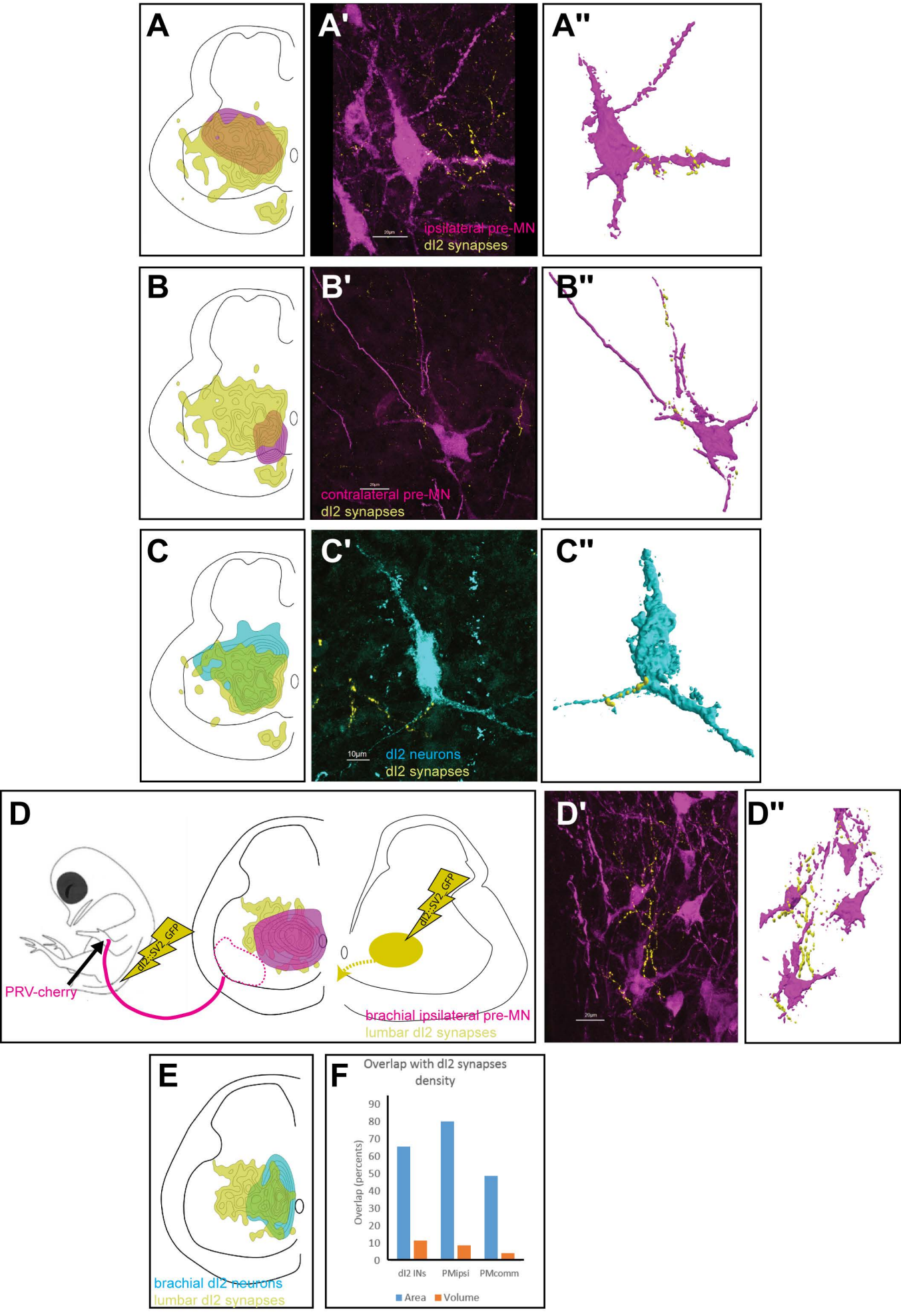

Fig. S8: Locomotion characteristics of control and TeTX-treated chicks.

A

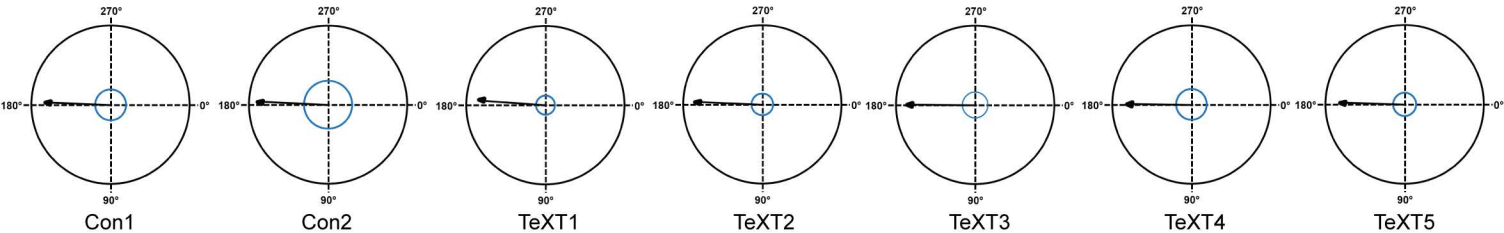
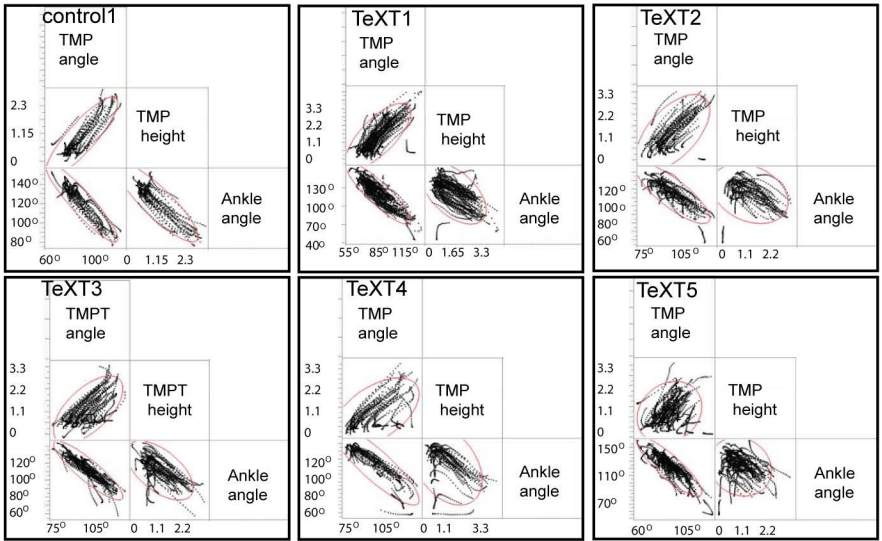
B